



Aeroelastic behavior of a composite plate-like wing under piezoelectrically induced stresses



Thiago de Souza Siqueira Versiani ^{a,b,*}, Douglas Quintanilha Tsunematsu ^b, Maurício Vicente Donadon ^a, Flávio José Silvestre ^c, Antônio Bernardo Guimarães Neto ^a, Alessandro Guimarães ^b

^a Instituto Tecnológico de Aeronáutica, São José dos Campos, SP 12228-900, Brazil

^b Instituto de Pesquisas Tecnológicas do Estado de São Paulo, São José dos Campos, SP 12247-016, Brazil

^c Technische Universität Berlin, Berlin 10623, Germany

ARTICLE INFO

Article history:

Received 22 November 2019

Received in revised form 21 February 2020

Accepted 7 March 2020

Keywords:

Stress stiffening
Piezoelectric transducers
Aeroelastic stability
Composite structures
Finite elements

ABSTRACT

Recent aircraft are increasingly presenting unconventional wing configurations, resulting in unusual aeroelastic responses and consequently giving rise to different technological strategies to enhance aeroelastic stability. Among them, the technique of stress stiffening by piezoelectric actuation emerged as a promising technological solution to improve the aeroelastic stability of structures with both ends axially constrained. Therefore, an aeroelastic model employing smart composite beam elements and time domain aerodynamic loads with strip theory for stress stiffening aeroelastic problems was developed and carefully validated. In addition, the effect of bending-torsion coupling provided by concentrated masses on the aeroelastic response of the structure is also taken into account, which was included by the presence of a slender ballast arbitrarily positioned along the span and chord. Parametric studies were performed investigating the influence of aspect ratio, fiber orientation angle, ballast position, as well as piezoelectric unit position along the span and its input voltage. Results showed a promising performance of such technique, as it could increase the bandwidth of two flexible modes associated with the flutter mechanism.

© 2020 Elsevier Ltd. All rights reserved.

1. Introduction

Undesirable structural vibrations are a common problem present in mechanical systems, either due to direct external excitations or loss of dynamical stability. In aeronautics, flutter arises as one of the most critical dynamic instability phenomena, given the large number of structural collapses caused by it in history. In recent years, many researchers have concentrated their efforts in the study of the mechanism of this phenomenon and proposed different solutions to minimize its effects.

Specially for the most recent generation of aircraft, which is characterized by the relative low weight, the aeroelastic phenomena are more susceptible to occur due to the high flexibility of the structures. It is important to mention that the characteristic of low weight is highly desirable in aeronautical industry because of the performance enhancement, lower

* Corresponding author at: Instituto Tecnológico de Aeronáutica, São José dos Campos, SP 12228-900, Brazil.

E-mail address: versiani@ita.br (Thiago de Souza Siqueira Versiani).

pollutants emission, higher endurance and so on. Then, technological solutions in order to augment the stability and guarantee the safety of such aircraft are a constant challenge for engineers.

Among the technological devices used for stabilization, those which make use of piezoelectric transducers have drawn special attention due to their relative easy applicability, frequency of operation, low weight, speed of actuation and general good performance. It is easy to find many works which study different strategies that use such transducers in order to improve structural stability, specially in the aeronautical field. A specific application of piezoelectric transducers has been studied in recent years, which consists in subjecting a host structure to piezoelectrically induced stresses in order to change its mechanical behavior and, in turn, its stability and dynamic characteristics for different purposes, e.g., buckling enhancement [1–3] and natural frequencies tuning [3–7].

Among the works that considered beam models, Waisman and Abramovich [5] studied numerically the effect of piezoelectrically induced stresses on the flexible modes of a composite beam, taking into account the percentage of beam length covered by the transducers, as well as the lengthwise position, different applied voltages, boundary conditions and laminate layups. They observed that non-symmetric laminates are more sensitive to stress stiffening than symmetric ones. Moreover, the frequencies of the modes are directly proportional to the piezoelectric force. As a next step, the authors performed a similar study considering two sets of lead zirconate titanate (PZT) actuators, providing more control options of natural frequencies and mode shapes [6]. Kuo [7] proposed a closed-form solution of a piezoelectrically induced stresses problem in a composite beam and performed modal analyses for different PZT positions, covered lengths and applied voltages. The author observed that the system is more sensitive to decreasing the stiffness than to increasing it. Another important contribution of his work is the optimal position of the actuators, which consists in attaching them at the high bending/shear regions for achieving a better performance by decreasing/increasing the natural frequencies of the respective flexible mode. Kulinski and Przybylski [3] observed that a beam is more sensitive to stress stiffening effects when the bending rotation degree of freedom is free at the boundaries.

As observed in the aforementioned works, piezoelectrically induced stresses play an important role in tuning natural frequencies of slender structures. Taking advantage of this feature, one can improve the aeroelastic stability of flexible structures by suitably tuning natural frequencies and then increasing the flutter velocity. Considering this point of view, Kasem and Dowell [8] studied the aeroelastic response of a smart plate-like wing of low aspect ratio for different configurations of actuators positions. The results showed an excellent improvement in the flutter velocity, with an expressive percentage increase. Moreover, the torsional modes showed to be more affected by increasing or decreasing piezoelectric forces than bending modes. In another work, Kasem et al. [9] studied the effect of the geometric stiffness provided by piezoelectric actuators on the aeroelastic response of smart composite wings. Different configurations of actuators positions were analyzed and it was concluded that distributing piezoelectric patches along the wing span improve even more the aeroelastic stability than attaching them at the wing root. Moreover, an increase of 26.9% in the divergence speed and 34.3% in the flutter speed were obtained. In the two last cited works [8,9], aeroelastic analyses of a plate-like wing which take into account piezoelectrically induced stresses were for the first time studied. However, only low aspect ratio structures with clamped-free boundary conditions were addressed. As it could be seen in many of the previously cited works [1–3,5–7], structures axially constrained at both boundaries are more sensitive to stress stiffening effects.

If we take a look at the literature about the new generation of aircraft, highlighting flexible aircraft, we can see that there are high aspect ratio structures with both ends axially constrained, where the applicability of piezoelectrically induced stresses could become a potential technique for aeroelastic stability improvement. For example, it could be a starting point the improvement of the aeroelastic stability of truss-braced wings, specially for the truss that connects the middle part of the wing to the fuselage, as in the SUGAR aircraft illustrated in Fig. 1a; or even for each segment of box-wings (see Fig. 1b). It is possible to see that, in this latter case, there are engines which provide bending-torsion coupling to the respective part of the wing which surely affect the aeroelastic stability of the structure.

As can be seen, the effect of piezoelectrically induced stresses on the aeroelastic stability of high aspect ratio composite structures with both ends axially constrained was not addressed in any of the aforementioned works. Specially when the coupling contribution of additional devices attached to the structure (as engines, missiles, actuators, sensors, etc) is taken into account. The present work is the first study addressing the aforementioned conceptual problem, which was investigated considering a smart idealized wing, i.e., a conceptual aeroelastic structure.

In summary, the present work aims at studying the aeroelastic behavior of a composite plate-like wing under piezoelectrically induced stresses and its sensitivity to different parameters change. The main scope of the paper is to evaluate the feasibility of improving the aeroelastic stability of a clamped-clamped composite structure using piezoelectrically induced stresses. A detailed parametric study taking into account geometry, composite lay-up, inertia parameters, position and prescribed voltage on the piezoelectric unit pair as well its effectiveness is presented in this paper aiming at a better understanding of the effects of the piezoelectrically induced stress on the aeroelastic stability of the piezoaeroelastic plate-like wing.

2. Formulation and modeling

In order to represent the previously discussed aeroelastic system, consider a rectangular composite plate-like wing clamped at both ends, as illustrated in Fig. 2, where V_∞ is the undisturbed flow velocity.



(a) SUGAR (Adapted, [10])



(b) Lockheed Martin box-wing aircraft design [11]

Fig. 1. New concept aircraft. (See above-mentioned references for further information.)

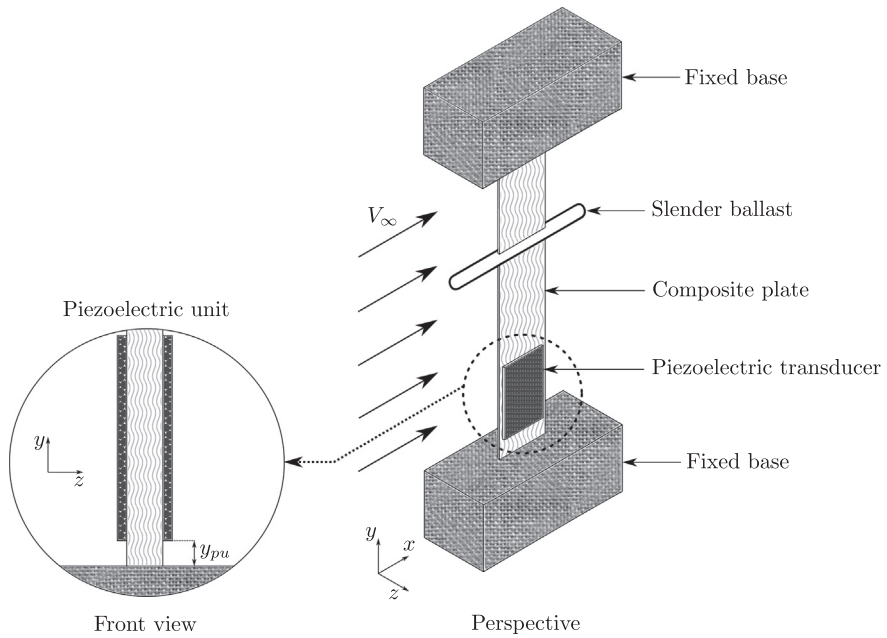


Fig. 2. Aeroelastic system.

The aeroelastic system is composed by piezoelectric transducers attached on both surfaces at arbitrary positions along the span of a thin composite plate. In this paper, the set of piezoelectric transducers will be called *piezoelectric unit* and its span-wise position will be described by y_{pu} . Moreover, a slender ballast is attached to the plate and can be placed at different positions along the span and chord in order to provide different levels of bending-torsion coupling.

The equations of motion of the structural model are derived by employing the principle of stationary total potential energy and the solution of the equations are approximated by the finite element method employing two-node eight-degree-of-freedom smart beam elements, assuming small deflections and neglecting transverse shear effects.

Discretizing the structure in beam elements, two types of elements will be obtained: a beam element containing only the composite material and other also containing piezoelectric transducers attached to the top and bottom surfaces. In a general way, the smart composite element (see Fig. 3) can be formulated for all the structure and then the piezoelectric transducers width can be set to zero where they are not present. In the case where the slender ballast is present, its inertial contribution is simply included.

2.1. Kinetic energy

The kinetic energy of the system under study can be described by:

$$T = T_{cp} + T_{sb} \quad (1)$$

where T_{cp} is the kinetic energy of the composite plate, which encompasses piezoelectric and composite materials, and T_{sb} is the kinetic energy of the slender ballast.

The displacement field of the structure under study accounts for axial, bending and torsion motions. The bending was formulated assuming the Euler-Bernoulli kinematic relations [12]. The torsion, in turn, was formulated assuming the Saint-Venant torsion theory [13].

Consider the reference system as illustrated in Fig. 3 and assume that u , v and w are the displacements of the neutral axis in the x , y and z directions, respectively. It is important to note that w is defined as positive downward, opposite to the z axis. Hence, assuming that α is the torsion angle around the y axis, the displacement field $\{r_{cp}\}$ of the composite plate can be written as:

$$\{r_{cp}\} = \begin{Bmatrix} z\alpha \\ v - zw_y \\ -w - x\alpha \end{Bmatrix}. \quad (2)$$

Therefore, the kinetic energy of the composite plate can be described by [12]:

$$T_{cp} = \frac{1}{2} \int_{\Omega} \{r_{cp}\}^T \{r_{cp}\} \rho d\Omega, \quad (3)$$

where Ω is the spatial domain that encompasses the composite plate and piezoelectric transducers and ρ is the respective material density.

The Eq. (3) can be integrated only along the x direction (associated with the structure width) and the terms can be grouped with respect to each degree of freedom and the coupling terms. Moreover, assuming that the cross section is symmetric with respect to the z axis, we obtain:

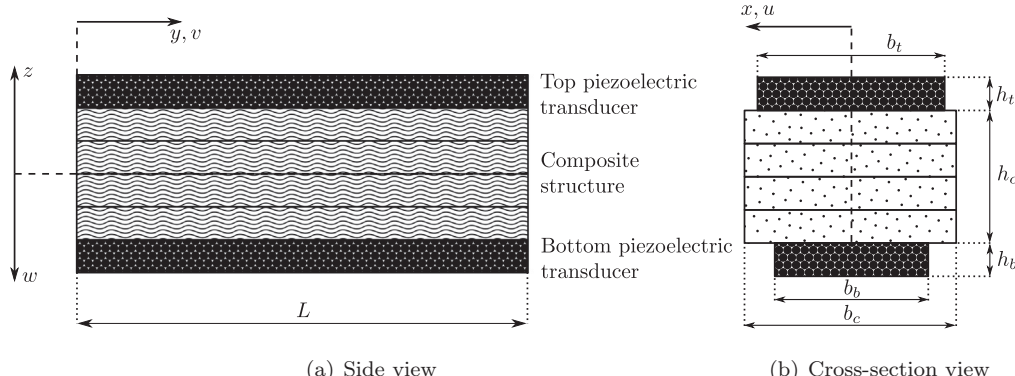


Fig. 3. Smart composite element.

$$\begin{aligned}
T_{cp} = & \frac{1}{2} \int_0^L \left[\underbrace{\left(\rho_t b_t \int_{h_t} dz + \rho_c b_c \int_{h_c} dz + \rho_b b_b \int_{h_b} dz \right) \dot{v}^2}_{I_{vv}} \right. \\
& - 2 \underbrace{\left(\rho_t b_t \int_{h_t} zdz + \rho_c b_c \int_{h_c} zdz + \rho_b b_b \int_{h_b} zdz \right) \dot{v} \dot{w}_y}_{I_{v\theta}} \\
& + \underbrace{\left(\rho_t b_t \int_{h_t} z^2 dz + \rho_c b_c \int_{h_c} z^2 dz + \rho_b b_b \int_{h_b} z^2 dz \right) \dot{w}_y^2}_{I_{\theta\theta}} \\
& + \underbrace{\left(\rho_t b_t \int_{h_t} zdz + \rho_c b_c \int_{h_c} zdz + \rho_b b_b \int_{h_b} zdz \right) \dot{w}^2}_{I_{ww}} \\
& + \left(\rho_t \left(b_t \int_{h_t} z^2 dz + \frac{b_t^3}{12} \int_{h_t} dz \right) \right. \\
& + \rho_c \left(b_c \int_{h_c} z^2 dz + \frac{b_c^3}{12} \int_{h_c} dz \right) \\
& \left. \left. + \rho_b \left(b_b \int_{h_b} z^2 dz + \frac{b_b^3}{12} \int_{h_b} dz \right) \right) \dot{\alpha}^2 \right] dy
\end{aligned} \tag{4}$$

where $\rho_{(t,c,b)}$, $b_{(t,c,b)}$ and $h_{(t,c,b)}$ are the density, width and thickness of the top piezoelectric transducer, composite plate and bottom piezoelectric transducer, respectively; and $\int_{(h_t, h_c, h_b)}$ represents a contracted notation for:

$$\begin{aligned}
\int_{h_t} &= \int_{\frac{h_c}{2}}^{\frac{h_c}{2} + h_t} \\
\int_{h_c} &= \int_{-\frac{h_c}{2}}^{\frac{h_c}{2}} \\
\int_{h_b} &= \int_{-h_b}^{\frac{h_c}{2}}.
\end{aligned} \tag{5}$$

Similarly, the kinetic energy associated with the slender ballast motion, which is modeled as a concentrated mass m_{sb} , can be described by:

$$\begin{aligned}
T_{sb} = & \frac{1}{2} m_{sb} (\dot{v}(\bar{y}))^2 + \frac{1}{2} m_{sb} (\dot{w}(\bar{y}))^2 \\
& + m_{sb} \bar{x} \dot{w}(\bar{y}) \dot{\alpha}(\bar{y}) + \frac{1}{2} (m_{sb} \bar{x}^2 + I_{yy_{sb}}) (\dot{\alpha}(\bar{y}))^2,
\end{aligned} \tag{6}$$

where $I_{yy_{sb}}$ is the moment of inertia around the y axis. The variables \bar{x} and \bar{y} denote the position of the ballast center of mass along the plate chord and span, respectively.

Substituting Eqs. (4) and (6) in Eq. (1), we obtain the total kinetic energy described by:

$$T = \frac{1}{2} \int_0^L \left\{ \begin{array}{c} \dot{v} \\ \dot{w} \\ \dot{\theta} \\ \dot{\alpha} \end{array} \right\}^T \underbrace{\begin{bmatrix} I_{vv} & \cdot & -I_{v\theta} & \cdot \\ \cdot & I_{ww} & \cdot & \cdot \\ -I_{v\theta} & \cdot & I_{\theta\theta} & \cdot \\ \cdot & \cdot & \cdot & I_{xx} \end{bmatrix}}_{[Im_{cp}]} \left\{ \begin{array}{c} \dot{v} \\ \dot{w} \\ \dot{\theta} \\ \dot{\alpha} \end{array} \right\} dy + \frac{1}{2} \left\{ \begin{array}{c} \dot{v}(\bar{y}) \\ \dot{w}(\bar{y}) \\ \dot{\theta}(\bar{y}) \\ \dot{\alpha}(\bar{y}) \end{array} \right\}^T \underbrace{\begin{bmatrix} m_{sb} & \cdot & \cdot & \cdot \\ \cdot & m_{sb} & \cdot & \bar{x}m_{sb} \\ \cdot & \cdot & \cdot & \cdot \\ \cdot & \bar{x}m_{sb} & \cdot & \bar{x}^2 m_{sb} + I_{yy_{sb}} \end{bmatrix}}_{[Im_{sb}]} \left\{ \begin{array}{c} \dot{v}(\bar{y}) \\ \dot{w}(\bar{y}) \\ \dot{\theta}(\bar{y}) \\ \dot{\alpha}(\bar{y}) \end{array} \right\}, \tag{7}$$

where $\theta = w_y$ and the dot notation (\cdot) used in the matrices indicates that the respective term is equal to zero.

2.2. Potential energy

The potential energy of a unidimensional electromechanical system performing bending and torsion motions can be described by [14]:

$$\Pi = \frac{1}{2} \int_{\Omega} \sigma \varepsilon d\Omega - \frac{1}{2} \int_{\Omega} D E d\Omega + \frac{1}{2} \int_0^L G J_x \alpha_y^2 dy, \quad (8)$$

where σ is the mechanical stress; D the electrical displacement; E the electrical field; G is the shear modulus; J_x the torsion constant of the cross section; and ε is the mechanical strain associated with axial and bending motions, which is described by:

$$\varepsilon = \varepsilon_L + \varepsilon_{NL} \quad (9)$$

where ε_L and ε_{NL} are the linear and non-linear terms of the von Kármán strain-displacement relation [4,15,16], which are in the case of the present work described by Eqs. (10) and (11), respectively.

$$\varepsilon_L = v_y - z W_{yy} \quad (10)$$

$$\varepsilon_{NL} = \frac{1}{2} w_y^2 \quad (11)$$

The constitutive relations of linear piezoelectricity are defined by [17]:

$$\sigma = Q^E \varepsilon - e E \quad (12)$$

$$D = e \varepsilon + \xi^E E, \quad (13)$$

where Q^E is the elasticity modulus at constant electric field, e the piezoelectric constant and ξ^E the dielectric constant at constant strain. Substituting Eqs. (9), (12) and (13) in Eq. (8) and neglecting the high order term associated with ε_{NL} , we obtain:

$$\begin{aligned} \Pi = & \underbrace{\frac{1}{2} \int_{\Omega} Q^E (\varepsilon_L)^2 d\Omega}_{\textcircled{1}} - \underbrace{\int_{\Omega} e E (\varepsilon_L) d\Omega}_{\textcircled{2}} - \underbrace{\frac{1}{2} \int_{\Omega} \xi^E E^2 d\Omega}_{\textcircled{3}} \\ & + \underbrace{\frac{1}{2} \int_0^L G J_x \alpha_y^2 dy}_{\textcircled{4}} + \underbrace{\int_{\Omega} (Q^E \varepsilon_L - e E) \varepsilon_{NL} d\Omega}_{\textcircled{5}} \end{aligned} \quad (14)$$

Observing each term of Eq. (14), we see that the term $\textcircled{1}$ describes the mechanical strain energy associated with the axial and bending motions; $\textcircled{2}$ describes the potential energy which arises from the electromechanical coupling; $\textcircled{3}$ describes the electrical potential energy; $\textcircled{4}$ describes the mechanical strain energy associated with torsion motion; and $\textcircled{5}$ represents the electromechanical strain energy associated with the piezoelectrically induced pre-stresses [1,4,18].

Assuming that the piezoelectric transducer can be approximated by an ideal capacitor, the relation between the internal electrical field E_{pzt} and the electrical potential difference ϕ_{pzt} between the electrodes can be described by [17]:

$$E_{pzt} = -\frac{\phi_{pzt}}{h_{pzt}}$$

where h_{pzt} is the piezoelectric transducer thickness and the subscript 'pzt' describes a general piezoelectric transducer, which in the case of this work, can be the top ($pzt = t$) or bottom ($pzt = b$) one.

Substituting Eqs. (10), (11) and (15) in Eq. (14) and grouping the terms according to each degree of freedom and the coupling terms, we obtain:

$$\Pi = \int_0^L \left[\frac{1}{2} \begin{Bmatrix} v_y \\ w_y \\ \theta_y \\ \alpha_y \end{Bmatrix}^T \left(\begin{bmatrix} A & \cdot & -B & \cdot \\ \cdot & \cdot & \cdot & \cdot \\ -B & \cdot & D & \cdot \\ \cdot & \cdot & \cdot & C \end{bmatrix} + \begin{bmatrix} \cdot & \cdot & \cdot & \cdot \\ \cdot & C_{NL} & \cdot & \cdot \\ \cdot & \cdot & \cdot & \cdot \\ \cdot & \cdot & \cdot & \cdot \end{bmatrix} \right) \begin{Bmatrix} v_y \\ w_y \\ \theta_y \\ \alpha_y \end{Bmatrix} - \begin{Bmatrix} v_y \\ w_y \\ \theta_y \\ \alpha_y \end{Bmatrix}^T \begin{bmatrix} [N] \\ \cdot \\ -[M] \\ \cdot \end{bmatrix} \begin{Bmatrix} \phi_t \\ \phi_b \end{Bmatrix} - \frac{1}{2} \begin{Bmatrix} \phi_t \\ \phi_b \end{Bmatrix}^T [C_{\phi\phi}] \begin{Bmatrix} \phi_t \\ \phi_b \end{Bmatrix} \right] dy \quad (16)$$

where the scalars A , B and D are expressed according to Eq. (17), and the terms $[N]$, $[M]$, $[C_{\phi\phi}]$ and C are described in Eqs. (18)–(20). In these equations, the terms $c_{(t,b)}$, $e_{(t,b)}$ and $\xi_{(t,b)}$ are the elastic modulus and the piezoelectric and dielectric constants of the top and bottom piezoelectric materials, respectively, and $a(i,j)$, $b(i,j)$ and $d(i,j)$ is the i -th row j -th column term of the inverse form of the respective $[A]$, $[B]$ and $[D]$ matrices calculated according to the classical lamination theory [12]. The

term $C_{NL} = A\varepsilon_p + B\kappa_p - [N]\{\phi_p\}$ is associated with the non-linear strain term of Eq. (14). The quantities ε_p and κ_p are calculated by solving the associated static problem [4,18] and describe the axial strain and curvature due to the piezoelectric unit actuation when a constant input voltage $\{\phi_p\}$ is prescribed.

$$(A, B, D) = \begin{Bmatrix} b_t \\ b_c \\ b_b \end{Bmatrix}^T \begin{Bmatrix} c_t \int_{h_t} (1, z, z^2) dz \\ \frac{1}{(\underline{a}(2,2), \underline{b}(2,2), \underline{d}(2,2))} \\ c_b \int_{h_b} (1, z, z^2) dz \end{Bmatrix} \quad (17)$$

$$([N], [M]) = \begin{Bmatrix} b_t \\ b_b \end{Bmatrix}^T \begin{bmatrix} \int_{h_t} (1, z) dz & \cdot \\ \cdot & \int_{h_b} (1, z) dz \end{bmatrix} \begin{bmatrix} e_t & \cdot \\ \cdot & e_b \end{bmatrix} \begin{bmatrix} -1/h_t & \cdot \\ \cdot & -1/h_b \end{bmatrix} \quad (18)$$

$$[C_{\phi\phi}] = \begin{bmatrix} -1/h_t & \cdot \\ \cdot & -1/h_b \end{bmatrix} \begin{bmatrix} b_t & \cdot \\ \cdot & b_b \end{bmatrix} \begin{bmatrix} \int_{h_t} dz & \cdot \\ \cdot & \int_{h_b} dz \end{bmatrix} \begin{bmatrix} \xi_t & \cdot \\ \cdot & \xi_b \end{bmatrix} \begin{bmatrix} -1/h_t & \cdot \\ \cdot & -1/h_b \end{bmatrix} \quad (19)$$

$$C = GJ_x \quad (20)$$

It is important to mention that the terms G and J_x of Eq. (20) take into account the top and bottom piezoelectric transducers contribution and are calculated according to Eqs. (21) and (22), respectively. The extensional stiffness matrix $[A^*]$ is calculated according to the classical lamination theory considering a laminate composed by composite and piezoelectric materials. Since in this case we take into account the piezoelectric laminae, the matrices calculated here are different from those obtained in Eq. (17), so an asterisk (*) was used to indicate this distinction.

$$G = \frac{1}{(h_t + h_c + h_b)\underline{a}^*(3, 3)} \quad (21)$$

$$J_x = \frac{1}{3} b_c (h_t + h_c + h_b)^3 \quad (22)$$

It is important to note that by using Eqs. (21) and (22), it is assumed that the piezoelectric transducers present the same width of the composite plate. Therefore, this approximation is necessary to take into account the contribution of the piezoelectric transducers in the equivalent torsional stiffness when they do not present the same width of the host structure, as illustrated in Fig. 3. Thus, the greater the width difference between them, the greater the error in modeling the torsion motion of the structure.

2.3. Aerodynamic loads

Consider an airfoil performing pitch and plunge motions, as described in Fig. 4, where b_s is the semi-chord and a is the percentage of b_s that describes the distance between the elastic axis and the center of the cross section. The pitch and plunge displacements of the airfoil are described respectively by α_a and w_a , which represent the aerodynamic degrees of freedom and might not be coincident with those formulated for the structural model. Nevertheless, the same coordinate system is adopted for both formulations and here w_a is also positive downward.

Using the W. P. Jones' approximation of the Wagner's function [19], the aerodynamic loads were modeled assuming unsteady aerodynamics and were applied to the system using the strip theory [14,20–22]. The aerodynamic force and

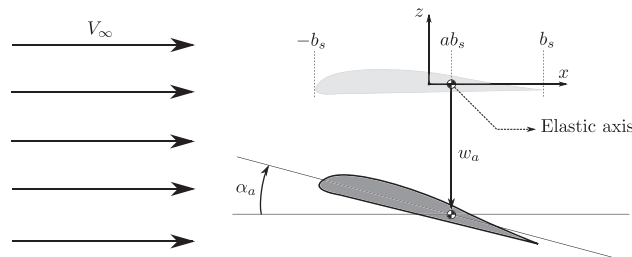


Fig. 4. Pitch and plunge motions of an airfoil.

moment per unit span applied to the structure can be described by Eqs. (23) and (24), respectively [23], where ρ_s is the air density and λ_1 and λ_2 are the lag states, whose dynamics is described in Eqs. (25) and (26).

$$\begin{aligned} L_{aer} = & 2\pi\rho_s b_s V_\infty \left[\left(\frac{b_s}{2V_\infty} \right) \ddot{w}_a - \left(\frac{ab_s^2}{2V_\infty} \right) \ddot{\alpha}_a + \dot{w}_a \right. \\ & \left. + b_s(1-a)\dot{\alpha}_a + V_\infty \alpha_a + \lambda_1 + \lambda_2 \right] \end{aligned} \quad (23)$$

$$\begin{aligned} M_{aer} = & 2\pi\rho_s b_s V_\infty \left[\left(\frac{ab_s^2}{2V_\infty} \right) \ddot{w}_a - \frac{b_s^3}{2V_\infty} \left(\frac{1}{8} + a^2 \right) \ddot{\alpha}_a + b_s \left(a + \frac{1}{2} \right) \dot{w}_a \right. \\ & \left. + ab_s^2 \left(\frac{1}{2} - a \right) \dot{\alpha}_a + b_s V_\infty \left(a + \frac{1}{2} \right) \alpha_a \right. \\ & \left. + b_s \left(a + \frac{1}{2} \right) \lambda_1 + b_s \left(a + \frac{1}{2} \right) \lambda_2 \right], \end{aligned} \quad (24)$$

$$\begin{aligned} \dot{\lambda}_1 = & -0.165\ddot{w}_a - 0.165b_s \left(\frac{1}{2} - a \right) \ddot{\alpha}_a - 0.165V_\infty \dot{\alpha}_a - 0.041 \frac{V_\infty}{b_s} \lambda_1 \\ \dot{\lambda}_2 = & -0.335\ddot{w}_a - 0.335b_s \left(\frac{1}{2} - a \right) \ddot{\alpha}_a - 0.335V_\infty \dot{\alpha}_a - 0.32 \frac{V_\infty}{b_s} \lambda_2 \end{aligned} \quad (26)$$

2.4. Modified Hamilton's Principle

The Modified Hamilton's Principle is defined by [24]:

$$\int_{t_1}^{t_2} (\delta T - \delta \Pi) dt - \int_{t_1}^{t_2} \sum_{i=1}^n Q_i \delta q_i dt = 0, \quad (27)$$

where n is the number of non-conservative external loads applied to the system, q is the generalized coordinate and Q_i is the generalized force, which is in this case composed by the aerodynamic loads acting on the structure and are described by Eqs. (23) and (24). In matrix notation, the generalized forces can be expressed by:

$$\begin{aligned} \{Q\} = \left\{ \begin{array}{l} -L_{aer} \\ M_{aer} \end{array} \right\} = & \underbrace{2\pi\rho_s b_s V_\infty \begin{bmatrix} \frac{-b_s}{2V_\infty} & \frac{ab_s^2}{2V_\infty} \\ \frac{ab_s^2}{2V_\infty} & \frac{-b_s^3}{2V_\infty} \left(\frac{1}{8} + a^2 \right) \end{bmatrix}}_{[A_1]} \left\{ \begin{array}{l} \ddot{w}_a \\ \ddot{\alpha}_a \end{array} \right\} \\ & + \underbrace{2\pi\rho_s b_s V_\infty \begin{bmatrix} -1 & -b_s(1-a) \\ b_s(a+\frac{1}{2}) & ab_s^2(\frac{1}{2}-a) \end{bmatrix}}_{[A_2]} \left\{ \begin{array}{l} \dot{w}_a \\ \dot{\alpha}_a \end{array} \right\} \\ & + \underbrace{2\pi\rho_s b_s V_\infty \begin{bmatrix} 0 & -V_\infty \\ 0 & b_s V_\infty (a+\frac{1}{2}) \end{bmatrix}}_{[A_3]} \left\{ \begin{array}{l} w_a \\ \alpha_a \end{array} \right\} \\ & + \underbrace{2\pi\rho_s b_s V_\infty \begin{bmatrix} -1 & -1 \\ b_s(a+\frac{1}{2}) & b_s(a+\frac{1}{2}) \end{bmatrix}}_{[A_4]} \left\{ \begin{array}{l} \lambda_1 \\ \lambda_2 \end{array} \right\} \end{aligned} \quad (28)$$

and the respective lag states dynamics by:

$$\begin{aligned} \left\{ \begin{array}{l} \dot{\lambda}_1 \\ \dot{\lambda}_2 \end{array} \right\} = & \underbrace{\begin{bmatrix} -0.165 & -0.165b_s(\frac{1}{2}-a) \\ -0.335 & -0.335b_s(\frac{1}{2}-a) \end{bmatrix}}_{[B_1]} \left\{ \begin{array}{l} \ddot{w}_a \\ \ddot{\alpha}_a \end{array} \right\} \\ & + \underbrace{\begin{bmatrix} 0 & -0.165V_\infty \\ 0 & -0.335V_\infty \end{bmatrix}}_{[B_2]} \left\{ \begin{array}{l} \dot{w}_a \\ \dot{\alpha}_a \end{array} \right\} \\ & + \underbrace{\begin{bmatrix} 0 & 0 \\ 0 & 0 \end{bmatrix}}_{[B_3]} \left\{ \begin{array}{l} w_a \\ \alpha_a \end{array} \right\} \\ & + \underbrace{\begin{bmatrix} -0,041 \frac{V_\infty}{b_s} & 0 \\ 0 & -0,32 \frac{V_\infty}{b_s} \end{bmatrix}}_{[B_4]} \left\{ \begin{array}{l} \lambda_1 \\ \lambda_2 \end{array} \right\} \end{aligned} \quad (29)$$

Defining vectors of structural and aerodynamic degrees of freedom as:

$$\{q\} = \begin{bmatrix} v & w & \theta & \alpha \end{bmatrix}^T \quad (30)$$

$$\{q_a\} = \begin{bmatrix} w_a & \alpha_a \end{bmatrix}^T \quad (31)$$

and vectors of electrical voltages and lag states as:

$$\{\phi\} = \begin{bmatrix} \phi_t & \phi_b \end{bmatrix}^T \quad (32)$$

$$\{\lambda\} = \begin{bmatrix} \lambda_1 & \lambda_2 \end{bmatrix}^T, \quad (33)$$

Eqs. (7), (16) and (28) can be substituted in Eq. (27) to obtain the structural dynamics of the aeroelastic system in a contracted notation, as described in Eq. (34). Since piezoelectric transducers will be used as actuators, the voltages applied to them are prescribed, and consequently, $\delta\phi_t$ and $\delta\phi_b$ are set to zero.

$$\int_{t_1}^{t_2} \int_0^L \left(\{\delta q\}^T [Im_{cp}] \{\ddot{q}\} + \{\delta q(\bar{y})\}^T [Im_{sb}] \{\ddot{q}(\bar{y})\} + \{\delta q_y\}^T ([C_{qq}] + [C_G]) \{q_y\} - \{\delta q_y\}^T [C_{q\phi}] \{\phi\} \right) dy dt \\ + \int_{t_1}^{t_2} \int_0^L ([A_1] \{\ddot{q}_a\} + [A_2] \{\dot{q}_a\} + [A_3] \{q_a\} + [A_4] \{\lambda\}) dy dt = 0 \quad (34)$$

The associated lag states dynamics stated in Eq. (29) can also be expressed in a contracted notation as described in Eq. (35).

$$\{\dot{\lambda}\} = \int_0^L ([B_1] \{\ddot{q}_a\} + [B_2] \{\dot{q}_a\} + [B_3] \{q_a\} + [B_4] \{\lambda\}) dy \quad (35)$$

2.5. Finite element method approximation

The composite plate-like wing illustrated in Fig. 2 was discretized in beam elements, accounting for axial, bending and torsion motions, as illustrated in Fig. 5.

The axial and torsion motions were interpolated by linear functions [25]. The bending, in turn, was interpolated by a cubic function [25]. Considering the interpolation functions of the mechanical degrees of freedom as $[N_q]$, we can write:

$$\{q\} = [N_q] \{q^e\}, \quad (36)$$

where the superscript $(\cdot)^e$ denotes that the respective degree of freedom is in the element level.

Substituting Eq. (36) in Eqs. (34) and (35), and considering the boundary conditions of the problem, the global equations of motion can be assembled. In this case, we obtain:

$$([M_{cp}] + [M_{sb}]) \{\ddot{q}^G\} + ([K_{qq}] + [K_G]) \{q^G\} - [K_{q\phi}] \{\phi^G\} = [G]^T [A_1] [G] \{\ddot{q}^G\} + [G]^T [A_2] [G] \{\dot{q}^G\} + [G]^T [A_3] [G] \{q^G\} \\ + [G]^T [A_4] \{\lambda^G\}, \quad (37)$$

$$\{\dot{\lambda}^G\} = [B_1] [G] \{\ddot{q}^G\} + [B_2] [G] \{\dot{q}^G\} + [B_3] [G] \{q^G\} + [B_4] \{\lambda^G\}, \quad (38)$$

where $[M_{cp}]$ is the composite plate mass matrix, $[M_{sb}]$ the slender ballast mass matrix, $[K_{qq}]$ the elastic stiffness matrix, $[K_G]$ the geometric stiffness matrix, $[K_{q\phi}]$ the piezoelectric stiffness matrix, $[G]$ the interpolation matrix from the structural to the

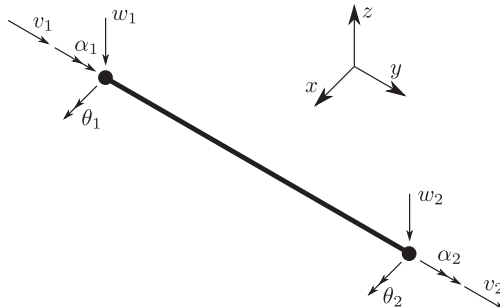


Fig. 5. Two-node eight-degree-of-freedom smart beam element.

aerodynamic degrees of freedom, and q^G , λ^G and ϕ^G are the global structural degrees of freedom vector, global lag states vector and global input voltages vector, respectively.

2.6. Geometric stiffness matrix calculation

In the case of the present study, the piezoelectric transducers are exclusively used for stress stiffening application. As discussed in Section 2.2, they are responsible for inducing an axial strain ε_p^G and a curvature κ_p^G which will be used for the calculation of the geometric stiffness matrix $[K_G]$ when a constant voltage $\{\phi_p^G\}$ is prescribed. It is important to note that, in Eq. (16), ε_p and κ_p are still unknown, and in the present step of modeling we will be able to calculate them.

For this calculation, it is necessary to solve the associated static problem neglecting the aerodynamic loads [4,18]. Therefore, Eq. (38) can be neglected and Eq. (37) reduces to Eq. (39), where the physical coordinates $\{q^G\}$ and actuators voltage $\{\phi_a^G\}$ are intentionally renamed to $\{q_p^G\}$ and $\{\phi_p^G\}$, indicating that they are now prescribed and are involved in a pre-stress problem.

$$[K_{qq}]\{q^G\} = [K_{q\phi}]\{\phi_a^G\} \Rightarrow \{q_p^G\} = [K_{qq}]^{-1}[K_{q\phi}]\{\phi_p^G\} \quad (39)$$

Once the piezoelectrically induced displacements $\{q_p^G\}$ is obtained, it is possible to calculate the strain state of the structure. The strain state of the element is given by:

$$\{\varepsilon_p^e\} = [N_{q,y}]\{q_p^e\}, \quad (40)$$

where $\{\varepsilon_p^e\}$ encompasses the axial strain ε_p^e and curvature κ_p^e .

According to Eq. (16), once the axial strain ε_p^e and curvature κ_p^e are obtained, the term C_{NL}^e (see Eq. (41)) is also obtained, and consequently, the geometric stiffness of the structure $[K_G]$ is calculated.

$$C_{NL}^e = A^e \varepsilon_p^e + B^e \kappa_p^e - [N^e]\{\phi_p^e\} \quad (41)$$

2.7. State-space realization form

As discussed in the previous section, the piezoelectric transducers are exclusively used for stress stiffening application. Once the geometric stiffness $[K_G]$ is obtained, it can be substituted in Eq. (37) and the piezoelectric stiffness matrix $[K_{q\phi}]$ can be conveniently neglected. In addition, grouping with Eq. (38) in a state-space realization form, we obtain:

$$\begin{Bmatrix} \{\dot{q}^G\} \\ \{\ddot{q}^G\} \\ \{\dot{\lambda}^G\} \end{Bmatrix} = \begin{bmatrix} [0]_{n_q \times n_q} & [I]_{n_q \times n_q} & [0]_{n_q \times n_\lambda} \\ -[M_t]^{-1}[K_t] & -[M_t]^{-1}[C_t] & [M_t]^{-1}[Q_4] \\ [D_3] - [D_1][M_t]^{-1}[K_t] & [D_2] - [D_1][M_t]^{-1}[C_t] & [B_4] + [D_1][M_t]^{-1}[Q_4] \end{bmatrix} \begin{Bmatrix} \{q^G\} \\ \{\dot{q}^G\} \\ \{\lambda^G\} \end{Bmatrix}, \quad (42)$$

where $[M_t]$, $[C_t]$ and $[K_t]$ are the apparent mass, damping and stiffness matrices, respectively; $[Q_4]$ expresses the lag states contribution to the dynamics; $[D_1]$, $[D_2]$ and $[D_3]$ express the contribution of the acceleration, velocity and displacement of the structure to the lag states dynamics, respectively; n_q describes the number of global structural degrees of freedom; and n_λ the total number of lag states. The aforementioned matrices are described from Eq. (43)–(47).

$$[M_t] = [M_{cp}] + [M_{sb}] - [G]^T[A_1][G] \quad (43)$$

$$[C_t] = [G]^T[A_2][G] \quad (44)$$

$$[K_t] = [K_{qq}] + [K_G] - [G]^T[A_3][G] \quad (45)$$

$$[Q_4] = [G]^T[A_4] \quad (46)$$

$$([D_1], [D_2], [D_3]) = ([B_1], [B_2], [B_3])[G] \quad (47)$$

3. Model validation

The proposed model was validated by parts according to each step of the modeling procedure. Therefore, the model validation is separated in structural dynamics, electromechanical, aeroelastic and geometric stiffness models, whose results were compared with others obtained from commercial softwares or those present in the literature.

3.1. Structural dynamic model

The structural dynamic model was validated performing the modal analysis of the proposed model for different configurations of laminate layup and considering the structure clamped at both ends. The natural frequencies for bending and torsion were compared with those calculated by the closed-form solution for beam structures [21].

It is important to mention that, in the case of composite structures, the use of the closed-form solution requires equivalent constants of Young modulus c for bending and shear modulus G for torsion. The equivalent shear modulus was calculated as described in Eq. (21) neglecting the piezoelectric transducers contribution, since in this case they will not be included. The equivalent Young modulus, in turn, was calculated according to Eq. (48), which extracts the desired constant from the extensional matrix $[A]$ calculated according to the classical lamination theory [12]. Note that the desired constant is related to the y axis, since it represents the longitudinal axis of the structure under study, as illustrated in Fig. 3.

$$c = \frac{1}{h_c a(2, 2)} \quad (48)$$

The mechanical system considered for simulation is a clamped-clamped composite woven glass-epoxy plate, whose constitutive properties are listed in Table 1 and physical parameters are described in Table 2. The structure was discretized in 70 beam elements with convergence reached.

The natural frequencies calculated by the closed-form solution and by the present model for the case of laminate layup $[(0, 90)_3]$ are described in Table 3. As can be seen, the natural frequencies calculated by the present model have an excellent agreement when compared to the exact solution.

In the case where the laminate presents the stacking sequence $[(-45, 45)_3]$, the natural frequencies calculated by the closed-form solution and by the present model are described in Table 4. Again, the natural frequencies calculated by the present model have an excellent agreement when compared to the exact solution.

Table 1
Constitutive properties of the woven glass-epoxy [4].

Property	Woven glass-epoxy lamina
Young modulus, c_{11} [GPa]	30.1
Young modulus, c_{22} [GPa]	30.1
Shear modulus, G_{12} [GPa]	5.5
Shear modulus, G_{13} [GPa]	5.5
Shear modulus, G_{23} [GPa]	5.5
Poisson's ratio, ν_{12}	0.14
Density, ρ [kg/m ³]	1905

Table 2
Parameters of the composite plate.

Parameter	Woven glass-epoxy lamina
Length [mm]	350
Width [mm]	30
Lamina thickness [mm]	0.235
Layups	$[(0, 90)_3]$ $[(-45, 45)_3]$

Table 3
Natural frequencies (Laminate layup: $[(0, 90)_3]$).

Mode	Bending		Torsion	
	Closed-form ^{*†}	Present model [*]	Closed-form ^{*†}	Present model [*]
1	23.5152	23.5151	114.0549	114.0644
2	64.8205	64.8200	228.1097	228.1863
3	127.0738	127.0720	342.1646	342.4231
4	210.0599	210.0540	456.2194	456.8323
5	313.7931	313.7799	570.2743	571.4715
6	438.2730	438.2474	684.3291	686.3985

[†] obtained from [21].

^{*} given in [Hz].

Table 4Natural frequencies (Laminate layup: $[(-45, 45)_3]$).

Mode	Bending		Torsion	
	Closed-form*†	Present model*	Closed-form*†	Present model*
1	17.5360	17.5360	176.7048	176.7196
2	48.3387	48.3384	353.4095	353.5282
3	94.7631	94.7617	530.1143	530.5148
4	156.6485	156.6441	706.8191	707.7686
5	234.0058	233.9960	883.5238	885.3787
6	326.8345	326.8154	1060.2286	1063.4347

† obtained from [21].

* given in [Hz].

3.2. Electromechanical model

The piezoelectric materials are able to transform energy between electrical and mechanical domains. Once these transducers are used as sensors (direct effect) or actuators (inverse effect), we can obtain as output signal an electrical voltage or mechanical strain, respectively [17]. In the case of the present work, the piezoelectric transducers are used only as actuators. Therefore, the inverse effect present in the model developed in Section 2 will be validated in this section.

Consider a cantilever bimorph beam composed by two layers of β -phase polyvinylidene fluoride (PVDF) of thickness h , as illustrated in Fig. 6. Its constitutive properties and physical dimensions are described in Table 5.

The structure model was discretized so that five identical bimorph patches of PVDF disposed along the beam length were obtained. The results were compared with those obtained by Suleman and Venkayya [26] and Hwang and Park [27].

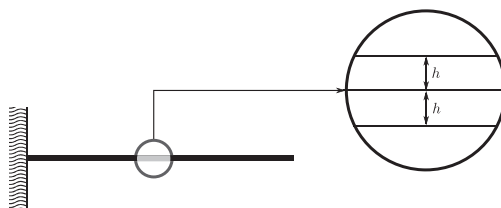
The inverse effect of the cantilever bimorph beam was checked by applying an input voltage equal to 1V as illustrated in Fig. 7, so that the transducers tend to bend the structure, and the vertical displacement was measured at different points along the beam length.

As depicted in Fig. 8, the results of the present model are in good agreement with those present in the literature.

3.3. Aeroelastic model

The aerodelastic model was validated considering a plate-like wing in clamped-clamped configuration, containing a ballast attached at the center of its span. Different ballast positions along the chord, called here as ballast offset, were investigated.

Aeroelastic analyses evaluating flutter speeds and frequencies for each case of ballast offset were compared with those obtained from a similar model developed in MSC Nastran employing beam elements, strip theory and the same Jones approximation of Wagner's function. Moreover, in MSC Nastran, the interconnection between the structural and the aerodynamic models was performed with beam splines, and the PK-method of flutter solution was used. It is important to mention that, due to the MSC Nastran requirements to simulate structures employing beam elements, an isotropic material was considered. The constitutive properties are $c = 68.2 \text{ GPa}$, $\nu = 0.33$ and $\rho = 2800 \text{ kg/m}^3$. The physical dimensions are

**Fig. 6.** Cantilever bimorph beam.**Table 5**

Constitutive properties and physical dimensions of the PVDF bimorph beam.

Young modulus, c [GPa]	2
Poisson's ratio, ν	0.29
Dielectric permittivity, ξ [pF/m]	106.2
Piezoelectric constant, e_{31} [$\text{N}/(\text{Vm})$]	0.046
Length, L [mm]	100
Width, b [mm]	5
Thickness, h [mm]	0.5

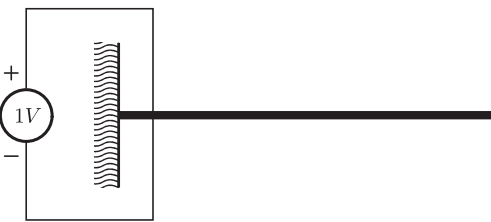


Fig. 7. PVDF transducers as actuators.

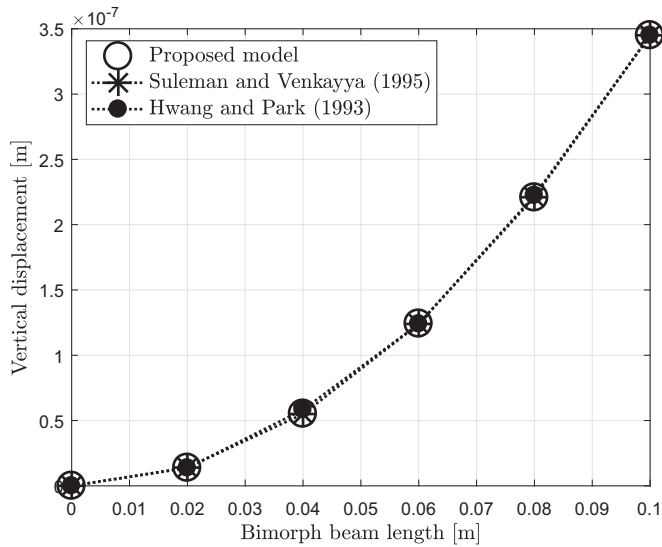


Fig. 8. Actuation validation.

$L = 350$ mm, $b = 30$ mm and $h = 0.705$ mm. The ballast is considered made of zinc-copper alloy with mass equal to 0.03458 kg and moment of inertia around y axis equal to 1.858×10^{-5} kg m². Moreover, both models were discretized in 70 elements with convergence reached.

As can be seen in Table 6, the flutter speeds and frequencies obtained with the present model are in excellent agreement with those calculated by MSC Nastran.

3.4. Geometric stiffness

Consider a bimorph beam composed only by piezoelectric transducers, as illustrated in Fig. 6. But now, instead of PVDF, consider the PZT as piezoelectric material. The constitutive properties and physical dimensions of the PZT bimorph beam are described in Table 7.

Table 6

Flutter speeds and flutter frequencies for different ballast offsets.

Ballast offset [mm]	Flutter speed [m/s]			Flutter frequency [Hz]		
	Present model	MSC Nastran	Error [%]	Present model	MSC Nastran	Error [%]
-20	99.60	100.10	-0.50	56.75	56.85	-0.18
-15	107.35	107.35	0.00	52.95	52.86	0.17
-10	140.35	140.10	0.18	50.04	49.84	0.40
-5	103.85	104.35	-0.48	30.17	30.14	0.10
0	69.60	69.85	-0.36	27.66	27.59	0.25
5	58.85	58.85	0.00	25.14	25.18	-0.16
10	52.35	52.35	0.00	22.85	22.91	-0.26
15	47.60	47.60	0.00	20.81	20.80	0.05
20	43.60	43.60	0.00	19.10	19.08	0.10

Table 7
Constitutive properties and physical dimensions of the PZT bimorph beam.

Young modulus, c [GPa]	69
Poisson's ratio, ν	0.30
Density, ρ [kg/m ³]	7700
Piezoelectric constant, e_{31} [N/(Vm)]	-12.351
Length, L [mm]	450
Width, b [mm]	20.574
Thickness, h [mm]	0.254

In this case, the effect of piezoelectrically induced stresses will appear only if the axial degree of freedom is restricted at the boundaries. Providing the same input voltage to top and bottom actuators so that both layers perform equal increasing deformations with no bending, a uniform distribution of stress is observed along the beam length if it is axially constrained at both ends.

According to the third Newton's law, the force applied on the beam by the reaction of the boundary constraint is analogous to an external force applied on the same beam when the piezoelectric transducers are not activated. If this force is high enough, the structure can buckle. With this in mind, we can calculate the necessary input voltage to buckle the structure using analytical solutions for buckling of structural members.

According to the Euler column buckling equation, the critical load P can be described by [28]:

$$P = \frac{\underline{\alpha} c I}{L^2}, \quad (49)$$

where I is the moment of inertia of the cross section and $\underline{\alpha}$ is a parameter which depends on the boundary conditions.

The stress provided by P is given by:

$$\sigma_p = \frac{P}{A} = \frac{\underline{\alpha} c I}{AL^2}, \quad (50)$$

where A is the cross section area of the beam.

Considering Eqs. (12) and (15), and that the structure is axially restricted so that no axial displacement is obtained, the resultant piezoelectric stress is given by:

$$\sigma_{pzt} = c z^0 + e \frac{\phi}{h} \quad (51)$$

As previously discussed, we can assume that the stress provided by an external mechanical load σ_p and by the piezoelectric actuation σ_{pzt} are equal. Equating Eqs. (50) and (51), we obtain the critical input voltage as:

$$\phi = \frac{\underline{\alpha} ch}{eAL^2} \quad (52)$$

Buckling analyses were performed for different boundary conditions with the axial degree of freedom restricted, which were in this case, one end clamped and other axially restricted, as illustrated in Fig. 9a; and both ends clamped, as illustrated in Fig. 9b. In both figures, it is depicted the buckling mode when the critical electrical voltage or the analogous mechanical load is applied, for the two boundary conditions.

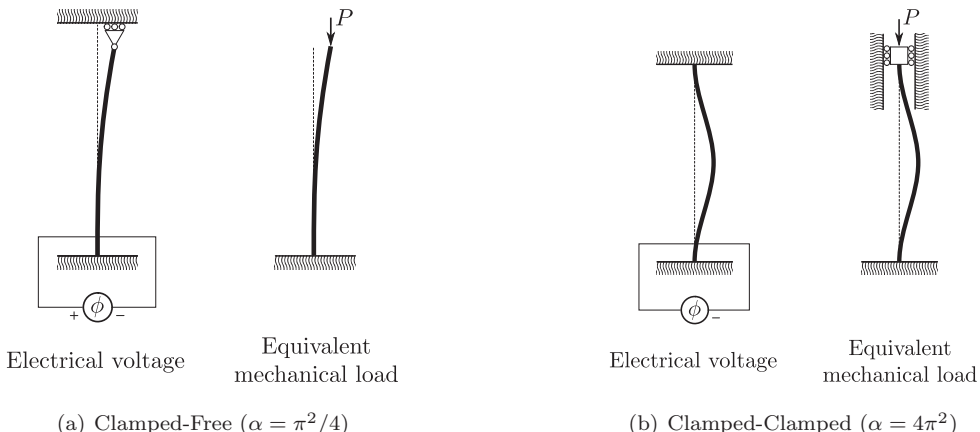


Fig. 9. Buckling validation.

When the critical voltage is applied to the system and the associated static eigenproblem is solved, the smallest eigenvalue is equal to unit. This means that the terms of $[K_G]$ associated with transversal stiffness become equal to those of $[K_{qq}]$ and, physically, the structure buckles due to the loss of stiffness. **Table 8** presents the critical input voltage calculated by Eq. (52) and the smallest eigenvalue obtained by solving the associated eigenproblem for each boundary condition considered for validation. As can be seen, the proposed model predicts exactly the geometric stiffness of the system.

4. Results and discussion

The aeroelastic response of the electromechanical system under study can be affected by many factors. Among them we can cite the aspect ratio, laminate layup, ballast spanwise position and its offset along the chord, the piezoelectric unit position along the span and the prescribed voltage. Therefore, parametric studies considering each of the aforementioned factors were carried out throughout this section in order to evaluate their influence on the modal and aeroelastic responses.

4.1. Aspect ratio and fibers orientation angle

The flexibility of the composite structure is directly related to its aspect ratio. According to the classical lamination theory, the stacking sequence can change the bending and torsional stiffnesses. Hence, it is expected that the modal and aeroelastic responses will be changed for different settings of such parameters.

Consider a woven glass-epoxy plate of width equal to 30 mm, lamina thickness equal to 0.235 mm and stacking sequence $[(\theta, \theta + 90^\circ)_3]$, where θ is the fibers orientation angle. The constitutive properties of the composite material are described in **Table 1**. Moreover, consider this plate clamped at both ends, with no piezoelectric transducers attached and with the ballast center of mass coincident with the center of the plate.

In order to obtain different aspect ratios (AR), the width and thickness were maintained constant, while the length was varied from 30 cm to 50 cm in steps of 5 cm. Calculating the first eight natural frequencies of the structure for the case of $\theta = 0^\circ$ and tracking their tendencies as θ is varied up to 90° in increments of 15° , we obtain the modal responses as illustrated in **Fig. 10**.

As can be seen, the frequencies of the flexible modes tend to decrease when the aspect ratio becomes higher, as it would be expected. However, bending modes are more affected than torsion modes, since low-frequency modes are increasingly dominated by bending modes as aspect ratio increases. In some cases, the bandwidth between some bending and torsion modes becomes relatively small, which may be undesirable for the aeroelastic stability of the structure.

The change in the fiber orientation angle from 0° to 45° gives rise to a decrease in the bending modes frequencies, whereas an increase in the torsion modes frequencies is observed. The symmetry with respect to $\theta = 45^\circ$ is due to the quasi-isotropic characteristic of the woven laminae and the stacking sequences considered. As observed for aspect ratio change, there are some cases of θ in which bending and torsion modes present very close frequencies. Moreover, as opposed to that observed for the aspect ratio, the change in fiber orientation angle provides more influence on the torsion modes than on the bending modes, specially for those which present higher frequencies.

It is important to note that, in all cases of aspect ratio and fibers orientation angle, the second symmetrical and asymmetrical torsion modes practically present the same frequency and the bandwidth between them is not affected by the parameters change.

Based on the modal response as a function of aspect ratio and fibers orientation angle obtained, the aeroelastic response of specific cases were chosen to be analyzed in detail. The selected cases were those of length equal to 30 cm and 50 cm and stacking sequence $[(0, 90)_3]$ and $[(-45, 45)_3]$.

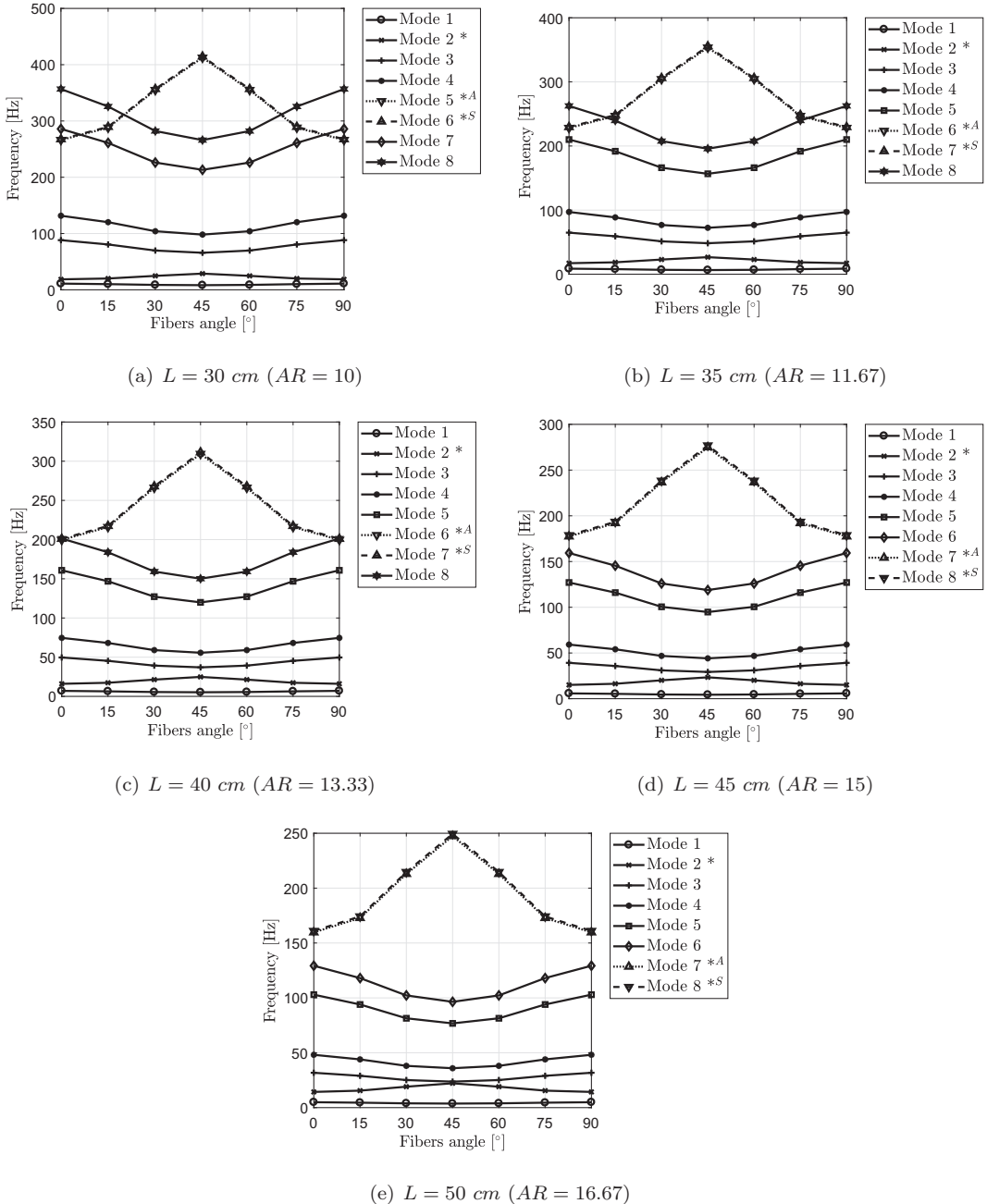
Starting with the aeroelastic analysis of the case where $L = 30$ cm and layup $[(0, 90)_3]$, we obtain the $V - g - f$ diagram and the root-locus as illustrated in **Fig. 11**.

Analyzing the $V - g$ diagram depicted in **Fig. 11b**, we observe a dynamic instability characterized by the vanishing of the system damping when the airspeed reaches the value of 30.1 m/s, which represents the flutter condition. As highlighted by the dash-dotted circle in the $V - f$ diagram depicted in **Fig. 11a**, the flutter mechanism is characterized by the two first flexible modes coupling, which are the first bending and first torsion modes as we can infer from **Fig. 10a**. Moreover, analyzing **Fig. 11c**, we can see that the pole which becomes unstable, giving rise to the flutter condition, is associated with the first torsion mode.

From **Fig. 11b** and c, we can see that the structure becomes statically unstable when the airspeed reaches the value of 51.85 m/s. Note that the divergence phenomenon is associated with a lag state, since its damping suddenly assumes a neg-

Table 8
Buckling load simulation.

Boundary condition	Critical voltage [V]	Smallest eigenvalue
Clamped-Free	0.744	1.00
Clamped-Clamped	11.898	1.00



* First torsion mode

^A Second asymmetrical torsion mode

^S Second symmetrical torsion mode

Fig. 10. Modal analysis as a function of aspect ratio and fibers orientation angle.

ative value [29]. In addition, it is important to note an interaction between one of the lag states and the first bending mode, which is highlighted by the dotted circle in Fig. 11a–c, indicating the emergence of a unique state with critically damped dynamics.

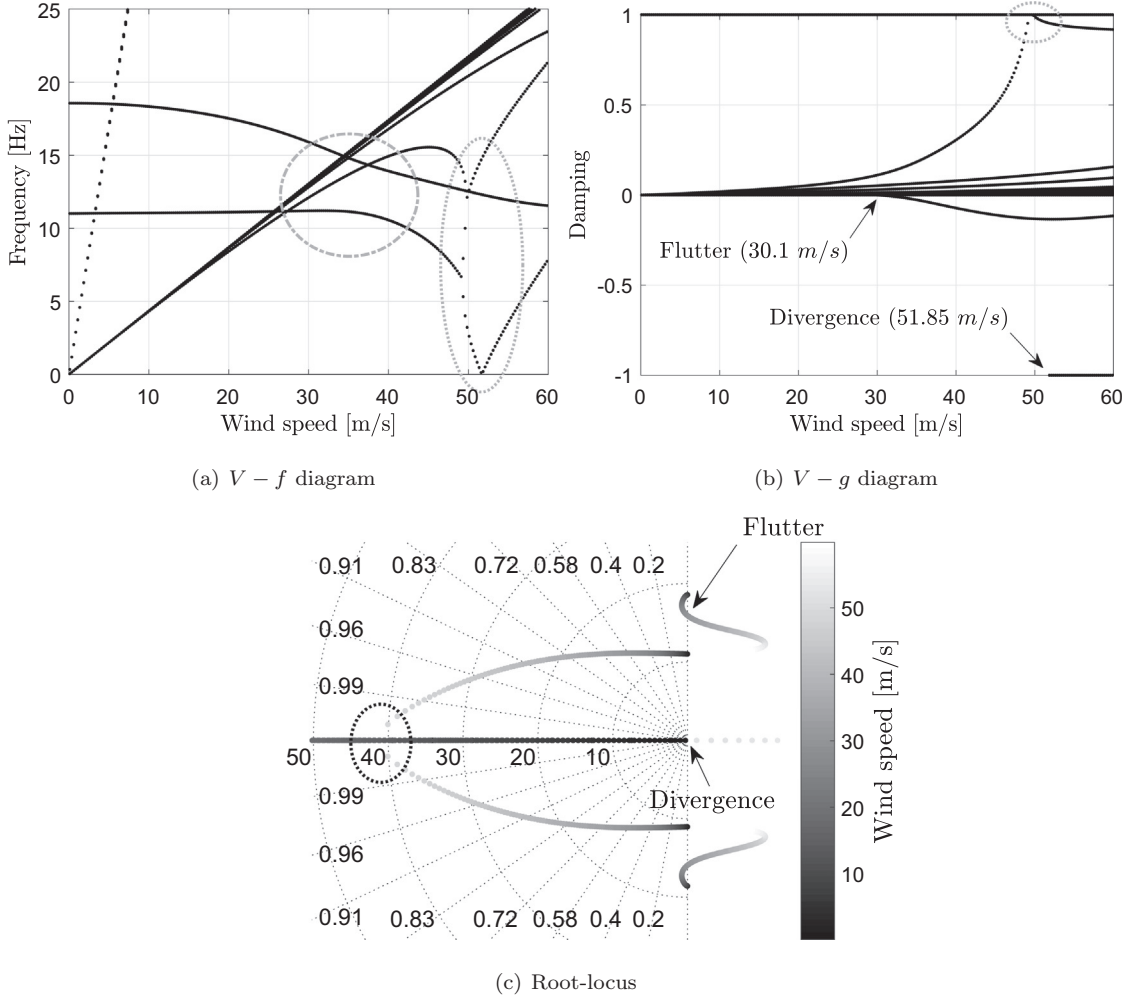


Fig. 11. Aeroelastic analysis for $L = 30$ cm and layup $[(0,90)_3]$.

If we simply change the fibers orientation angle, so that the layup $[(-45, 45)_3]$ is obtained, the flutter and divergence speeds are increased to 59.85 m/s and 80.1 m/s, respectively, as illustrated in Fig. 12. Note that the mechanism of flutter is still characterized by first bending and first torsion coupling with the unstable pole associated with the first torsion mode, as can be inferred from Fig. 12a and c in conjunction with Fig. 10a. Additionally, the interaction between one of the lag states and the first mode still occurs and is highlighted by the dotted circle.

Increasing the span length to 50 cm and considering again the stacking sequence $[(0,90)_3]$, we obtain the aeroelastic response depicted in Fig. 13. Comparing with the results illustrated in Fig. 11, we can see that by increasing the length of the structure the flutter and divergence speeds are decreased to 21.85 m/s and 31.1 m/s, respectively. However, the flutter mechanism did not change. Moreover, it is important to note that the interaction between one of the lag states and the first bending mode does not occur in this case.

Changing the fibers orientation angle in order to obtain the stacking sequence $[(-45, 45)_3]$, we obtain the aeroelastic response illustrated in Fig. 14. In this case, we can see that the change of laminate layup from $[(0,90)_3]$ to $[(-45, 45)_3]$ increases the flutter and divergence speeds, however they are lower than in the case of $L = 30$ cm (see Fig. 12). The mechanism of flutter is still characterized by first bending and first torsion coupling and the first mode interacts again with one of the lag states, giving rise to a unique state with critically damped dynamics, as highlighted by the dotted circles.

We see through the aforementioned cases that the aeroelastic response of the structure under study can be significantly affected by aspect ratio and fiber orientation angle changes. Bringing together the aeroelastic responses of all cases present in Fig. 10, we obtain the curves of flutter and divergence speed depicted in Fig. 15a and b, respectively.

In a general manner, we can observe a tendency of decreasing the flutter and divergence speeds when the aspect ratio becomes higher, for all cases of fiber orientation angle. Moreover, the change of the fiber orientation angle gradually increases the speeds, which present higher values when an angle of 45° is reached. It is important to note that the flutter

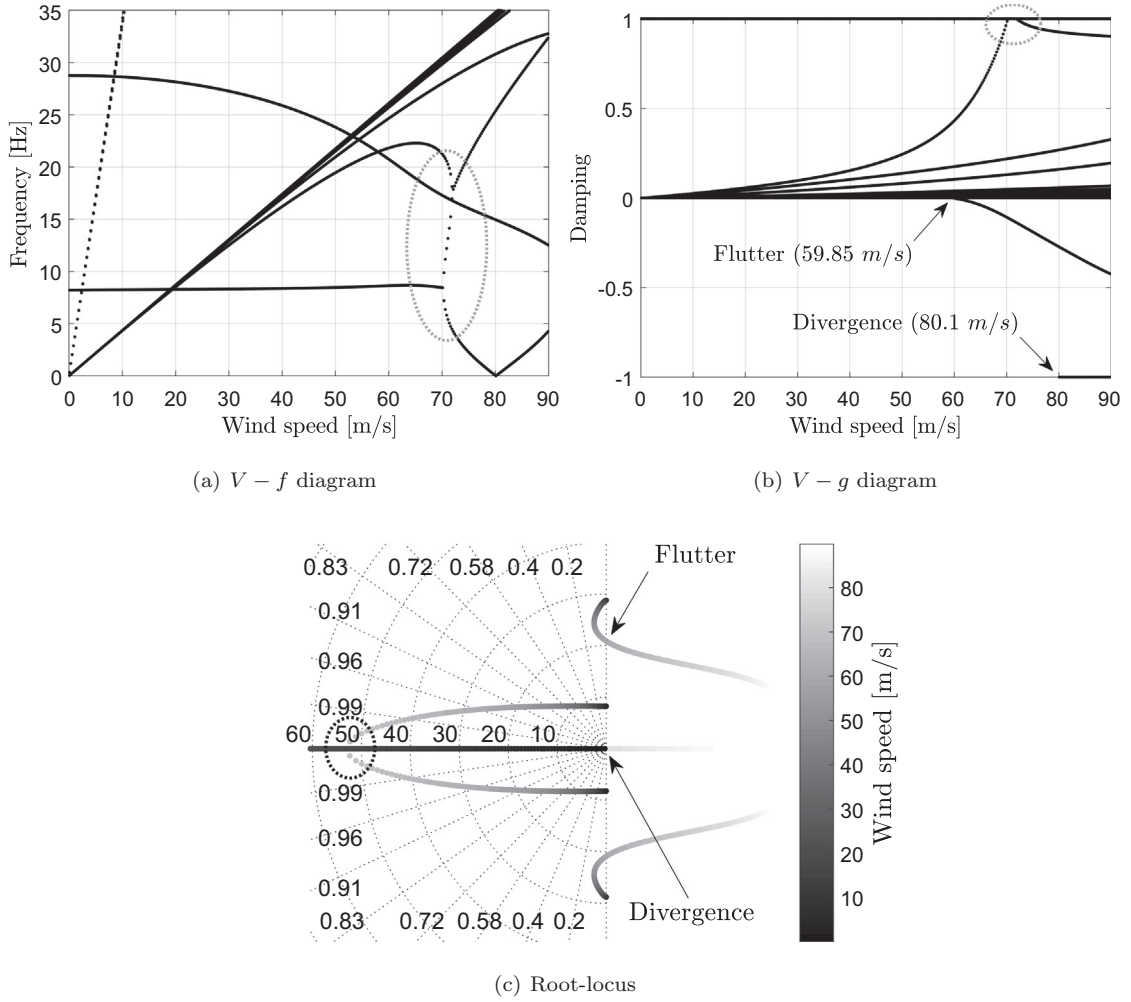


Fig. 12. Aeroelastic analysis for $L = 30$ cm and layup $[(-45, 45)_3]$.

and divergence curves present similar tendencies, whose symmetry is due to the quasi-isotropic characteristic of the woven laminae and the stacking sequences considered.

4.2. Ballast position along the span and offset along the chord

In this section, it will be investigated the influence of different positions of the ballast along the span and chord on the aeroelastic behavior of the structure. It is worth mentioning that the chordwise distance between the center of mass of the ballast and the elastic axis of the wing is called *offset* in this work. The ballast spanwise position will be varied in steps of 5 mm and the offset will be varied from -20 mm to 20 mm also in steps of 5 mm. It is important to emphasize that the results will not consider the frequencies when the ballast is exactly at the clamped regions, since it does not make physical sense to allocate it at such positions.

According to Figs. 11–14, the mechanism of flutter observed in these cases is characterized by the first bending and first torsion coupling. Therefore, in order to investigate the influence of the ballast position on the modes of lower natural frequency, the first four modes will be investigated. In addition, the modes under analysis can be identified with the help of Fig. 10.

4.2.1. Laminate $[(0, 90)_3]$

Considering the woven glass-epoxy plate-like wing with length equal to 350 mm and laminate layup $[(0, 90)_3]$, the modal analyses for each ballast position along the wingspan and chord are depicted in Fig. 16. Note that, in the cases with offset equal to ± 20 mm, the ballast center of mass is intentionally positioned out of the chord limits. Therefore, the surfaces presented in Fig. 16 do not depict the real dimension of the plate-like wing under analysis.

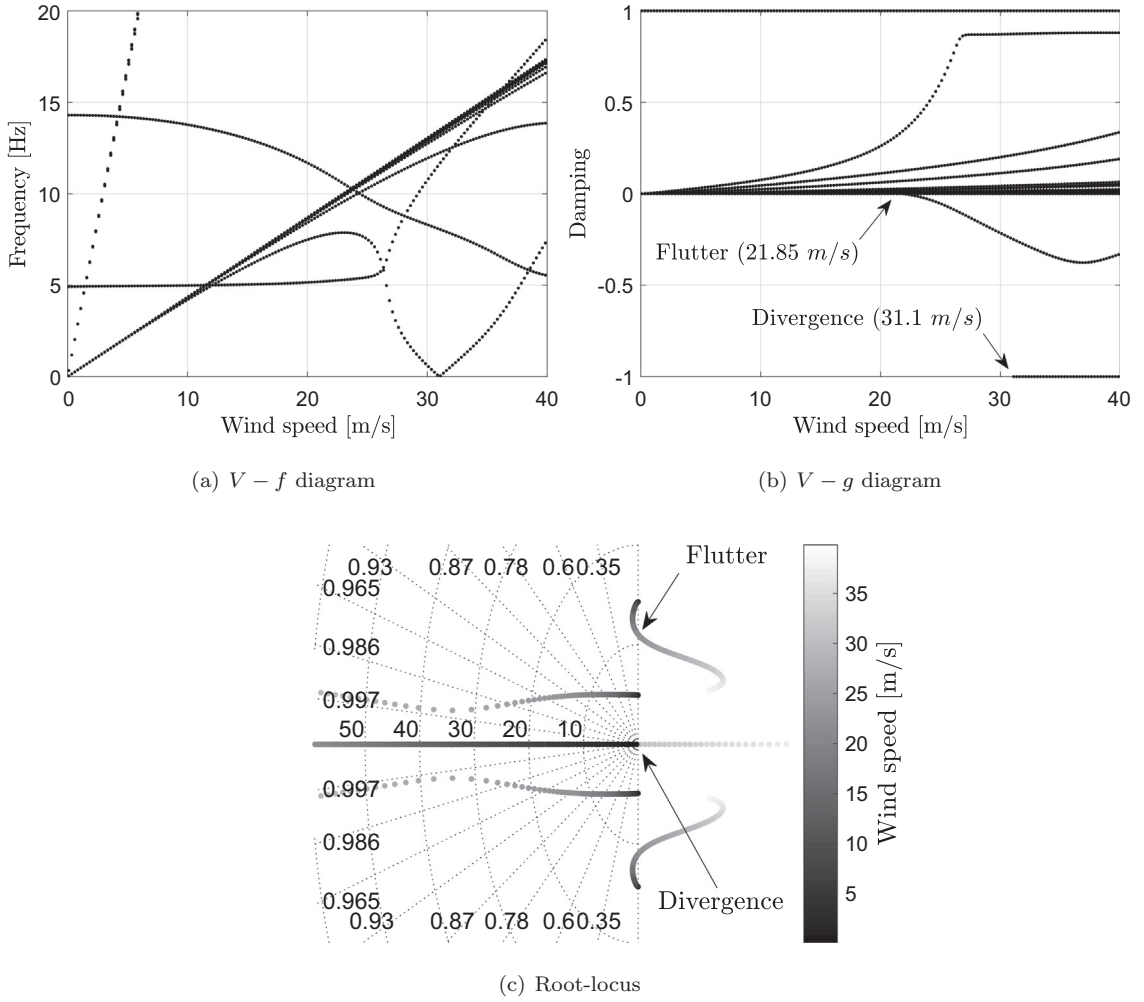


Fig. 13. Aeroelastic analysis for $L = 50$ cm and layup $[(0,90)_3]$.

According to Fig. 16a, the first bending mode can have its frequency significantly modified by allocating the ballast at different positions along the span, but it does not happen so expressively for different positions along the chord. As can be seen, the lowest frequency is obtained by allocating the ballast near the leading or trailing edges and around the center region of the wingspan. Moreover, it is important to note that a range of frequency around 16 Hz was obtained due to the change of the ballast position.

The torsion mode, in turn, does not have its frequency significantly modified by allocating the ballast at different spanwise and chordwise positions along the central region of the span, contrary to what is observed when allocated near the extremities, as can be seen in Fig. 16b. As observed for the first bending mode, the lowest frequency is also obtained by allocating the ballast around the center region of the wing. However, in this case, a range of frequency around 45 Hz was obtained due to the change of the ballast position.

In Fig. 16c and d, the regions close to the modal nodes are more sensitive to ballast position change along the span, while regions of high amplitudes of motion are more sensitive to offset changes. For both modes, the lowest frequencies are obtained by allocating the ballast at those regions of high amplitudes of motion, specially near the extremities. The highest frequencies, in turn, are obtained by allocating the ballast close to the modal nodes, becoming even higher when it is at the boundaries for the second bending mode and close to the central modal nodes for the third bending mode.

Performing an aeroelastic analysis of the structure for each position of the ballast along the span and chord, we obtain the flutter curve depicted in Fig. 17. As can be seen, the curve of flutter speed as a function of the ballast position presents a highly non-linear distribution, with a range of frequency around 60 Hz. The highest value of flutter speed is obtained when the ballast is allocated at the center of the wingspan and at the quarter-chord point, near the leading edge. The lowest values, in turn, are obtained by positioning the ballast towards the trailing edge, specially near the clamped regions.

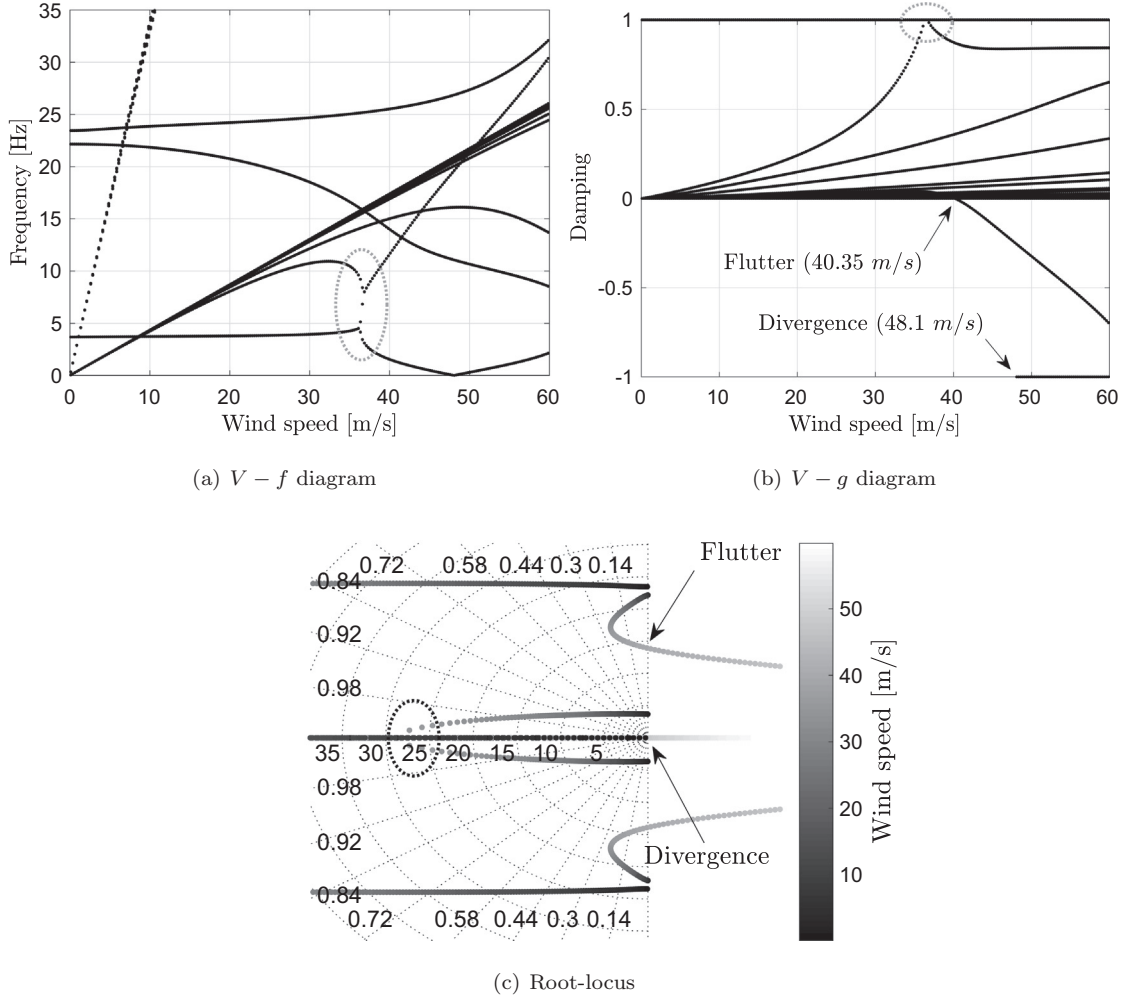


Fig. 14. Aeroelastic analysis for $L = 50$ cm and layup $[(-45, 45)_3]$.

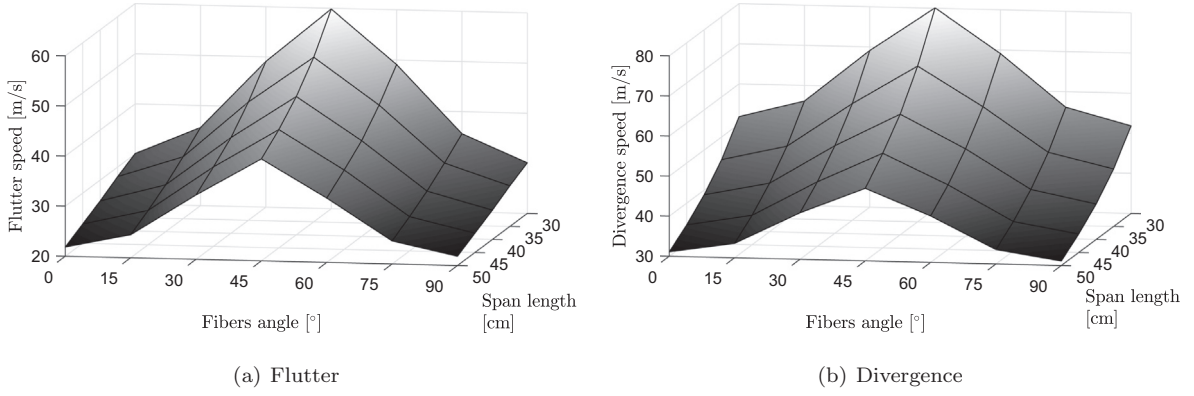


Fig. 15. Aeroelastic analysis as a function of span length and fibers orientation angle.

The flutter curve was assembled by performing an incremental procedure which is worth to be explained in detail: as the first step, the airspeed is set to a desired starting point, in this case, a value equal to 0.1 m/s. Then, the eigenvalues of the matrix of Eq. (42), which are the poles of the system, are calculated and analyzed. If there is no eigenvalue with positive real part, the airspeed is incremented, in this case, by a value equal to 0.25 m/s and the procedure returns to the poles calculation

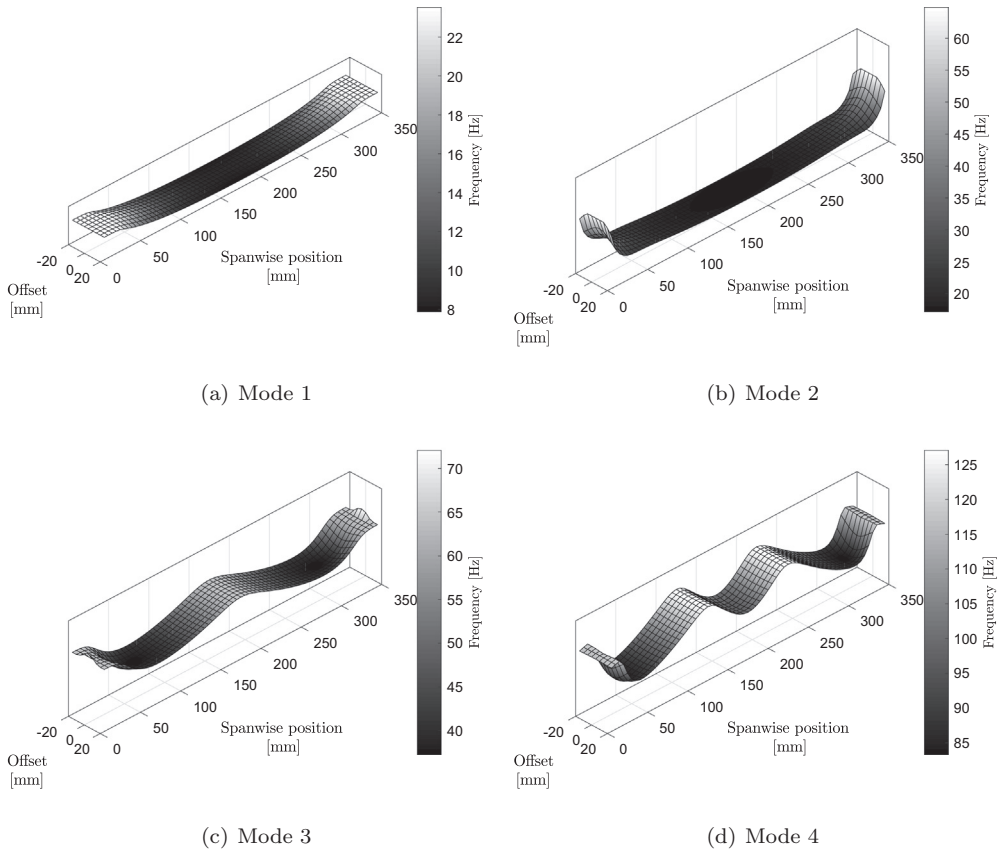


Fig. 16. Modal analysis for different ballast spanwise positions and offsets, considering $L = 35$ cm and layup $[(0, 90)_3]$.

step (no instability was detected). If there is at least one eigenvalue with positive real part (instability detected), the respective imaginary part needs to be analyzed. If the imaginary part is not null, the corresponding airspeed is labeled as flutter speed. If the imaginary part is null, a non-oscillatory instability is detected. This incremental procedure is summarized in flow chart form in Fig. 18.

One could expect that the detected non-oscillatory instability could be the static divergence. Since by definition the static divergence speed does not depend on the structure mass distribution [21–23], plotting the non-oscillatory instability speed as a function of the ballast position, it would be expected to observe the same speed for all cases. However, according to Fig. 19, we observe a constant speed of 44.35 m/s for almost all cases of ballast positions, and lower speeds when the ballast is positioned around the center region of the wingspan towards the trailing edge.

In order to evaluate one of these latter cases, consider the case in which the ballast is positioned at the center of the wingspan and at the trailing edge, i.e., with offset equal to 15 mm. Performing the aeroelastic analysis, we obtain the $V - g - f$ diagram and the root-locus as illustrated in Fig. 20.

According to Fig. 20c and d, we observe that as the airspeed increases, the pole that characterizes the flutter mechanism reaches the real axis on the right side of the complex plane before the pure real pole crosses the imaginary axis. Therefore, according to the previously described incremental procedure, the detected non-oscillatory instability is due to this already unstable pole, and not due to that associated with one of the lag states. It is important to note that this pole associated with one of the lag states crosses the imaginary axis at the same speed of 44.35 m/s as observed for most of the other cases of ballast position. Therefore, as observed in the aerelastic analyses performed in Section 4.1, this pure real pole is also associated with the static divergence phenomenon in the present case.

Analyzing the dynamics evolution of the pole associated with the flutter phenomenon, we can see that if the system were subjected to an airspeed lower than 18.85 m/s, it would present a damped oscillation towards the equilibrium state when disturbed. When subjected to an airspeed equal to 18.85 m/s, the system would present an undamped oscillation, i.e., it would be in a flutter condition. When subjected to an airspeed between 18.85 m/s and 42.1 m/s, the system would present an undamped oscillation, with growing period and amplitude as the airspeed increases. When subjected to an airspeed equal to 42.1 m/s, the system would present a divergent motion with no oscillation. However, since this instability is a mass dependent phenomenon, it does not consist in a static divergence. If the ballast were moved towards the leading edge, the system would present other configuration of mass distribution, and according to Figs. 17 and 19, the system could

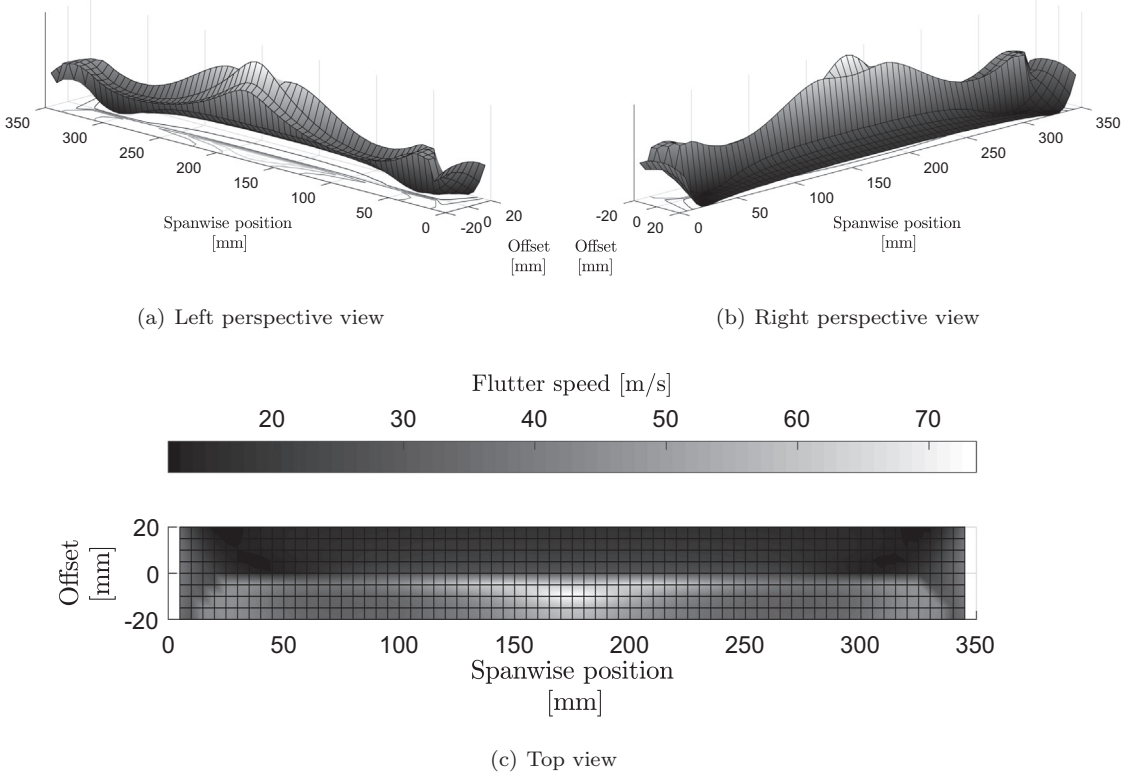


Fig. 17. Flutter speed for different ballast spanwise positions and offsets, considering $L = 35$ cm and layup $[(0, 90)_3]$.

become stable. Since, this phenomenon depends on the mass distribution of the system, it is a dynamic instability. We could say that the system would be in a *post-flutter divergence* condition.

As can be seen, in order to evaluate the aeroelastic response of structures similar to those under study in this work, the non-oscillatory instabilities have to be carefully analyzed.

4.2.2. Laminate $[(-45, 45)_3]$

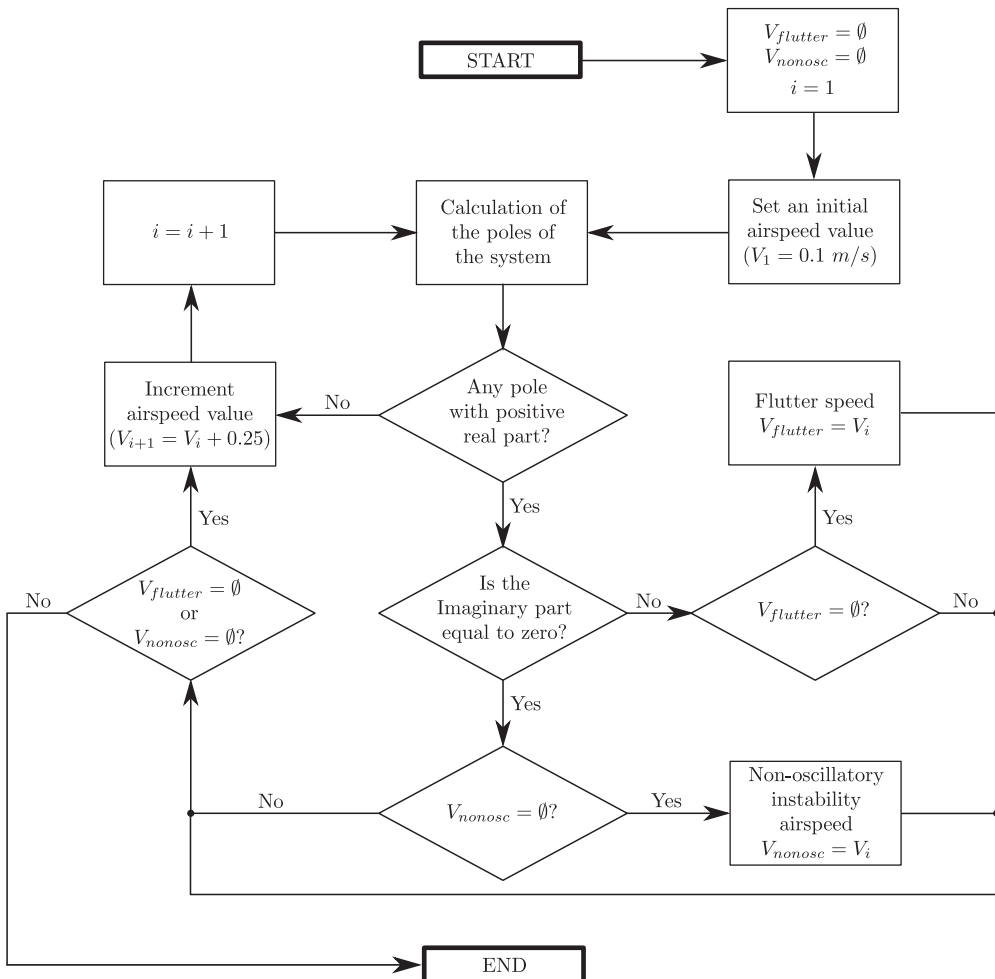
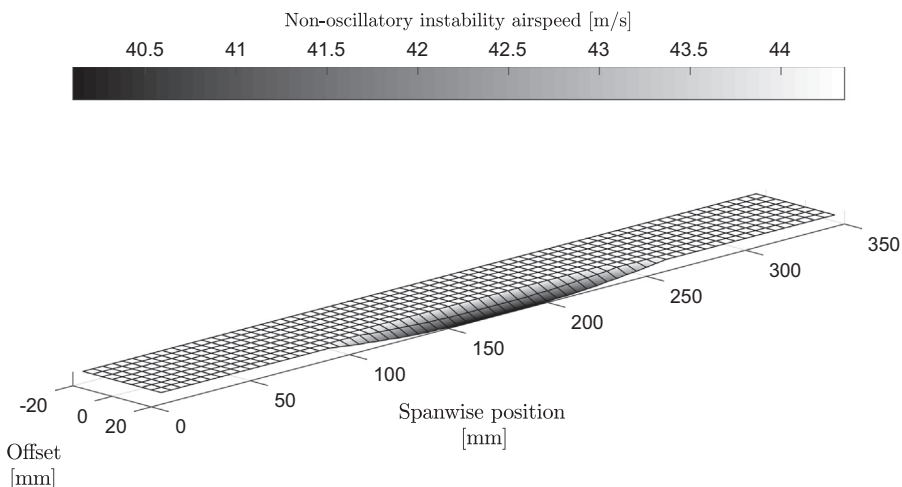
Changing the laminate layup to $[(-45, 45)_3]$, we obtain the modal response depicted in Fig. 21. As can be seen, the influence of the ballast position on the modal response is quite similar to the case in which the stacking sequence is $[(0, 90)_3]$, as depicted in Fig. 16. However, the ranges of frequency obtained in this case for the first bending and first torsion modes are around 12 Hz and 23 Hz, respectively, which are lower than those obtained in the case of laminate layup $[(0, 90)_3]$. Therefore, the first two flexible modes of the structure are more sensitive to the position of the ballast when the laminate layup is $[(0, 90)_3]$ than when it is $[(-45, 45)_3]$.

For the second and third bending modes, in turn, the ranges of frequency obtained are around 62 Hz and 50 Hz, respectively, which are higher than those obtained in the case of laminate layup $[(0, 90)_3]$. Therefore, the third and fourth flexible modes of the structure are more sensitive to the position of the ballast when the laminate layup is $[(-45, 45)_3]$ than when it is $[(0, 90)_3]$. Note that with the change of fiber orientation angle, these modes presented a higher difference between the frequencies when the ballast is positioned around the internal modal nodes and near the boundaries.

Generally, we can see that the modes have their frequencies significantly modified by allocating the ballast at different positions between modal nodes, specially at regions of high amplitude. This fact makes sense since regions of higher amplitudes are more sensitive to inertial contributions. Moreover, we can see that torsion modes are more sensitive to offset changes than bending modes.

In order to evaluate the aeroelastic response of the structure for the present layup case, the same incremental procedure described in Fig. 18 was performed for each ballast position along the span and chord.

Plotting the flutter speed as a function of ballast position along the span and chord, we obtain the curve depicted in Fig. 22. As can be seen, the distribution of the flutter speed for each case of ballast position also presents a highly non-linear distribution, with a range of frequency around 65 Hz. The highest flutter speeds are obtained when the ballast is allocated around the central region of the plate-like wing with an offset equal to -5 mm. However, the aeroelastic stability is highly compromised when the ballast is allocated at the central region of each half of the plate-like wing, also with negative values of offset.

**Fig. 18.** Incremental procedure for airspeed calculation of aeroelastic instabilities in flow chart form.**Fig. 19.** Non-oscillatory instability speed for different ballast spanwise positions and offsets, considering $L = 35$ cm and layup $[(0, 90)_3]$.

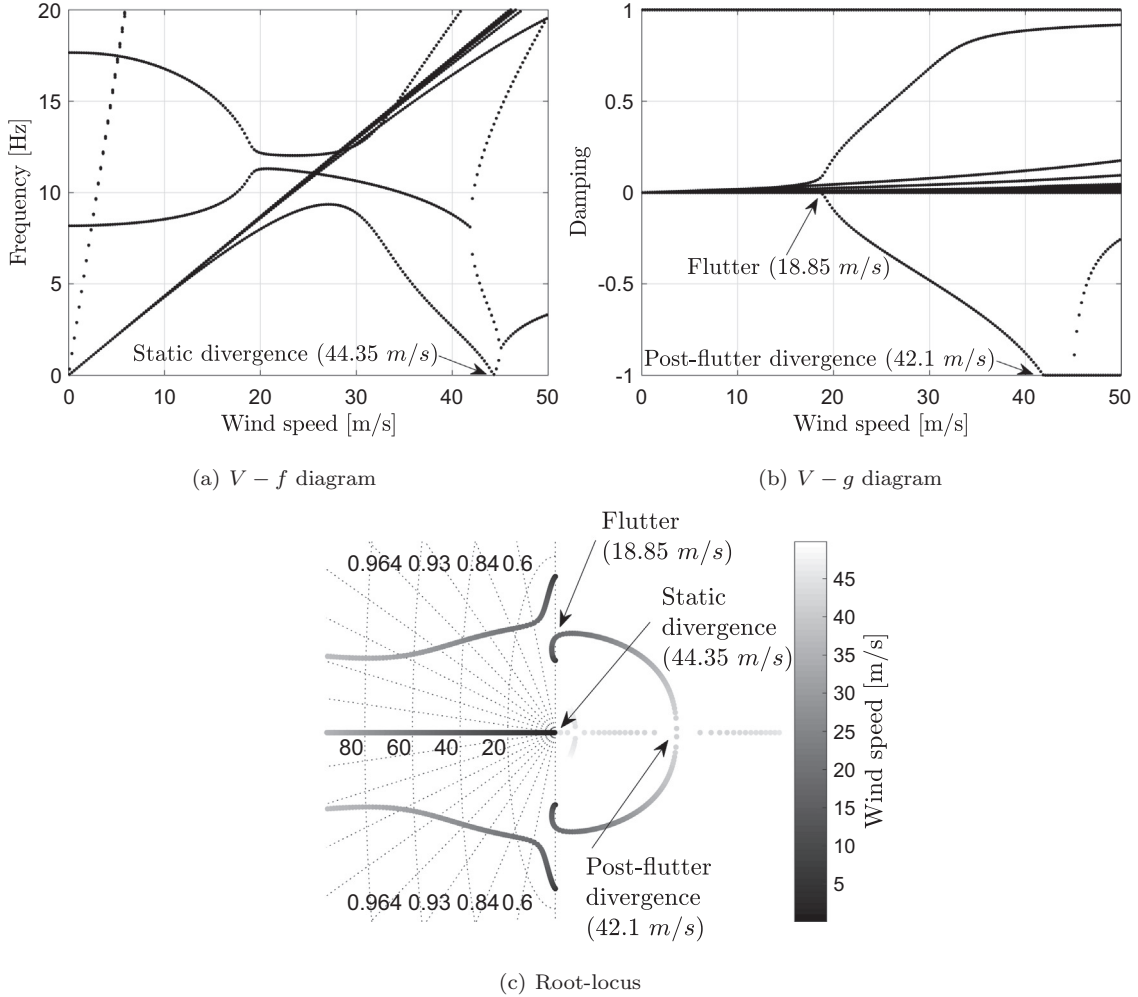


Fig. 20. Aeroelastic analysis for $L = 35$ cm, layup $[(0, 90)_3]$ and offset equal to 15 mm.

Analyzing the non-oscillatory instability response illustrated in Fig. 23, we can also observe a similar speed distribution to that presented by the case of laminate layup $[(0, 90)_3]$. However, for the present laminate layup under analysis, a higher number of cases of ballast position was obtained in which the *post-flutter divergence* presents a lower speed than the static divergence phenomenon.

4.3. Piezoelectric unit position and input voltage

Until this point, parametric studies varying aspect ratio, fibers orientation angle and ballast position along the wing span and chord were conducted.

In this section, it will be investigated the influence of piezoelectrically induced stresses on the modal and aeroelastic responses of the woven glass-epoxy plate-like wing under study, with physical dimensions and laminate layups considered in Section 4.2. For each case of laminate layup, the ballast center of mass will be allocated at the center of the wingspan with three cases of offset, -15 mm, 0 mm and 15 mm. The piezoelectric unit presents two transducers of length 45 mm, width 20.574 mm and thickness 0.254 mm, and is composed by PZT as piezoelectric material, whose constitutive properties are described in Table 7. The parametric study will be conducted varying the piezoelectric unit position (y_{pu} , see Fig. 2) along the span in steps of 5 mm, as well as the input voltage ϕ_{pu} from -200 V to 200 V in steps of 50 V.

From the aeroelastic responses presented in Figs. 11, 12, 13, 14 and 20, we could see that the flutter phenomenon occurs due to the first bending and first torsion modes coupling. Therefore, the modal response of the first two flexible modes will be investigated. Moreover, the incremental procedure presented in Fig. 18 will be performed for each piezoelectric unit position and prescribed voltage for all cases of laminate layup and ballast offset considered.

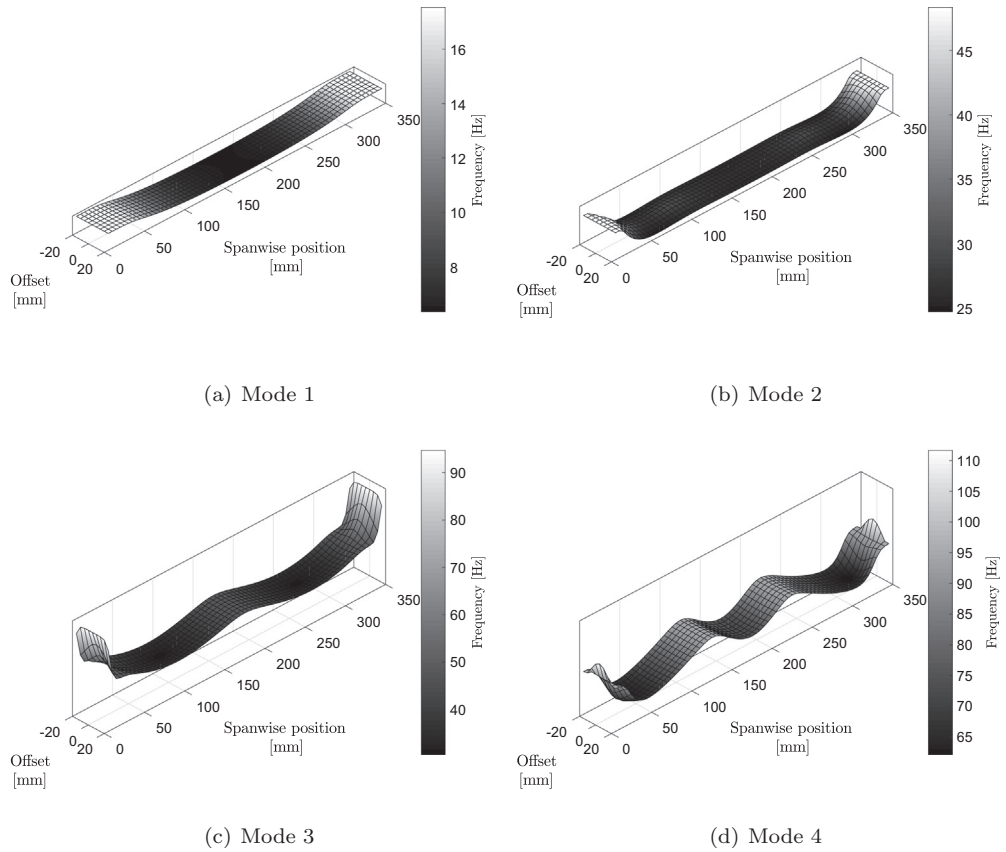


Fig. 21. Modal analysis for different ballast spanwise positions and offsets, considering $L = 35$ cm and layup $[(-45, 45)_3]$.

An inverse piezoelectric effectiveness parameter η is introduced to measure the effectiveness of the technique used to improve the aeroelastic stability, taking into account the relation between the percentage of flutter velocity increase over the percentage of the maximum piezoelectric energy provided by the piezoelectric unit [30], which is described by:

$$\eta = \frac{\Delta \bar{q}_{cr}}{\bar{U} \bar{q}_{cr}^{\phi_0}} = \frac{V_{cr}^{\phi_{pu}} - V_{cr}^{\phi_0}}{V_{cr}^{\phi_0}} \left(\frac{\phi_{max}}{\phi_{pu}} \right)^2, \quad (53)$$

where $\Delta \bar{q}_{cr} = \bar{q}_{cr}^{\phi_{pu}} - \bar{q}_{cr}^{\phi_0}$; $\bar{q}_{cr}^{\phi_{pu}}$ is the critical aerodynamic pressure calculated when a voltage ϕ_{pu} is applied to the piezoelectric unit, as well as $\bar{q}_{cr}^{\phi_0}$ when $\phi_{pu} = 0$; $V_{cr}^{\phi_{pu}}$ is the flutter speed associated to $\bar{q}_{cr}^{\phi_{pu}}$, as well as $V_{cr}^{\phi_0}$ to $\bar{q}_{cr}^{\phi_0}$; ϕ_{max} is the maximum voltage magnitude supported by the piezoelectric transducers, in this case, ± 200 V; $\bar{U} = (C_{pzt} \phi_{pu}^2 / 2) / (C_{pzt} \phi_{max}^2 / 2)$ in which C_{pzt} is the piezoelectric transducer capacitance. It is important to mention that the sign of ϕ_{max} depends on the sign of ϕ_{pu} , so that both must present the same sign.

4.3.1. Laminate $[(0, 90)_3]$

As first case, consider the laminate layup $[(0, 90)_3]$ and offset equal to 0 mm, whose modal and aeroelastic analyses are illustrated in Figs. 24 and 25, respectively.

According to Fig. 24a, we can see that for a constant value of voltage, the frequency of the first bending mode can be modified only by the change of the piezoelectric unit position. This occurs due to the local increase of stiffness and mass provided by the piezoelectric material. Since positive voltages induce compressive loads in the host structure due to the expansion of the piezoelectric transducers, the structure stiffness is significantly decreased, but not sufficiently to reach the buckling condition. In addition, a range of frequency of 8.90 Hz was obtained prescribing voltages from -200 V to 200 V.

According to Fig. 24b, the torsion mode is not affected by piezoelectrically induced stresses. It would be already expected because according to the piezoelectric effects modeling and since the torsion motion is uncoupled in the adopted kinematic relations, the piezoelectric unit induces only axial strains. Additionally, in this case of offset there is no ballast contribution to the bending-torsion coupling. However, the increase of local stiffness and mass due to the presence of the piezoelectric

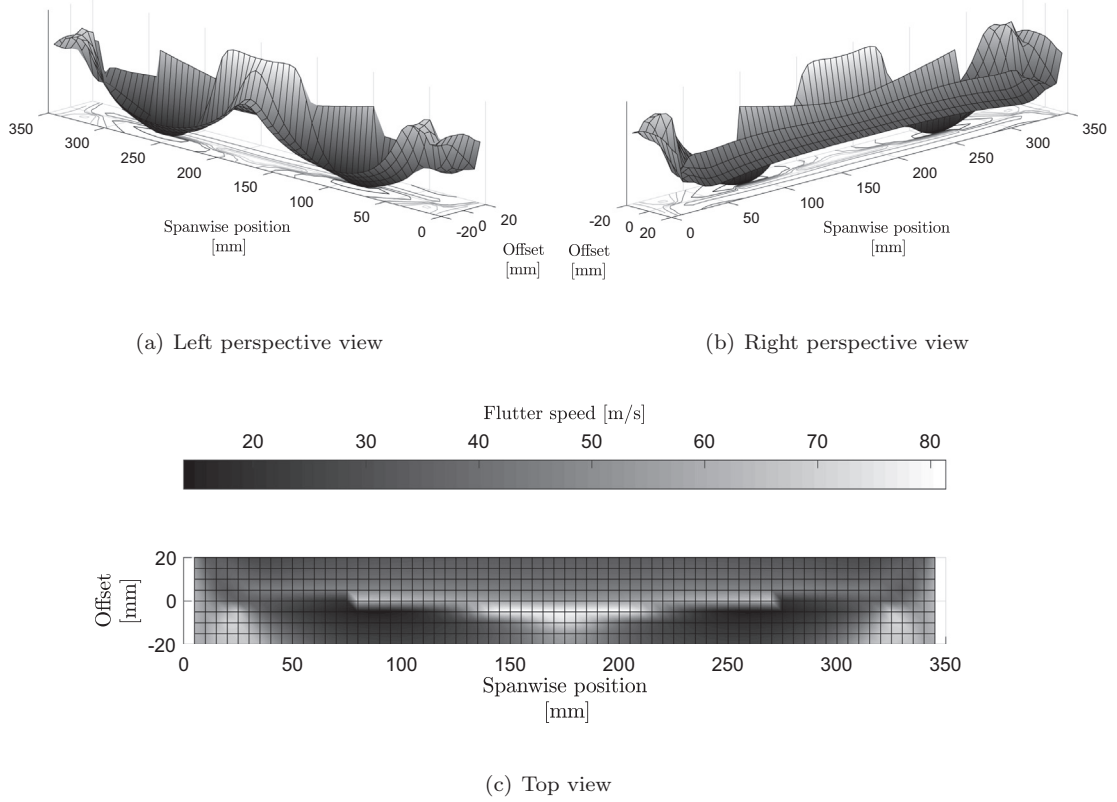


Fig. 22. Flutter speed for different ballast spanwise positions and offsets, considering $L = 35$ cm and layup $[(-45, 45)_3]$.

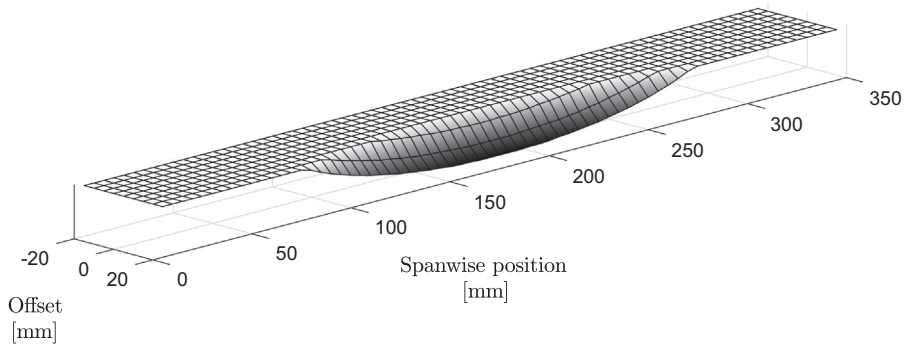
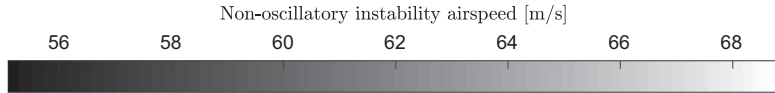


Fig. 23. Non-oscillatory instability speed for different ballast spanwise positions and offsets, considering $L = 35$ cm and layup $[(-45, 45)_3]$.

material is able to change the torsion frequency when the piezoelectric unit is allocated along the wingspan. In this case, a range of frequency of 0.29 Hz was obtained.

From Fig. 25a, we can see that the highest flutter speed is reached when the piezoelectric unit assumes the positions and prescribed voltages which correspond to the lowest first bending frequencies (see Fig. 24a). Since the torsion mode is not significantly affected by the piezoelectric unit (see Fig. 24b), the bandwidth between these modes is described by how low the first bending frequency can become. This same analysis can be made for the lowest flutter speeds, in which the

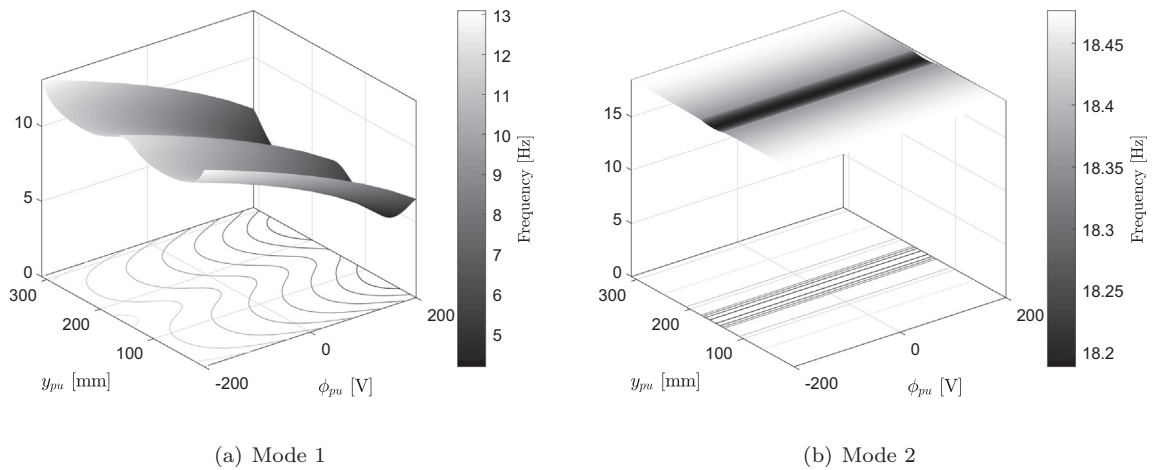


Fig. 24. Modal analysis for different piezoelectric unit spanwise positions y_{pu} and input voltages ϕ_{pu} , considering $L = 35$ cm, layup $[(0, 90)_3]$ and ballast located at the middle of the span with offset equal to 0 mm.

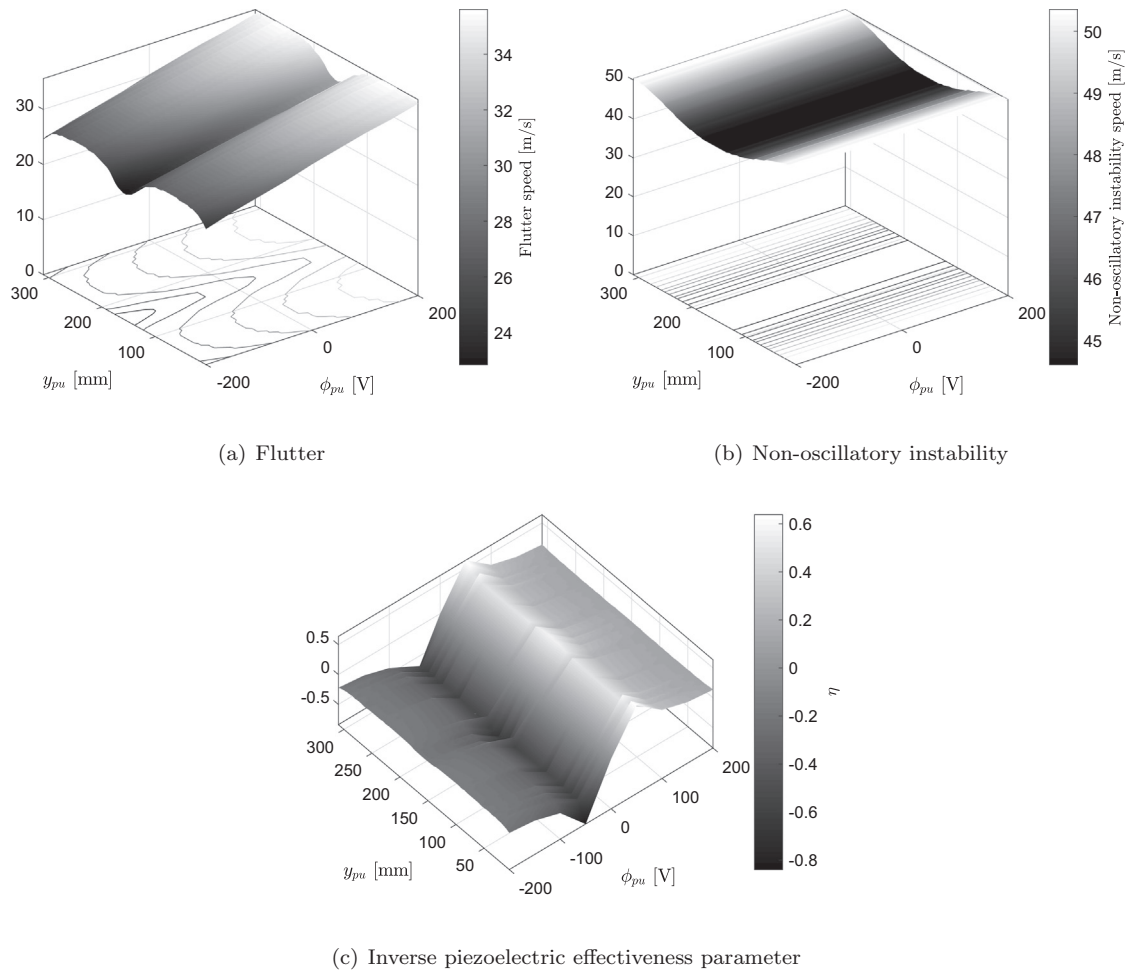


Fig. 25. Aeroelastic analysis for different piezoelectric unit spanwise positions y_{pu} and input voltages ϕ_{pu} , considering $L = 35$ cm, layup $[(0, 90)_3]$ and ballast located at the middle of the span with offset equal to 0 mm.

piezoelectric unit assumes the positions and prescribed voltages which correspond to the highest first bending frequencies. As can be seen, changing the piezoelectric unit position and prescribed voltage, we obtain a range of flutter speeds of 12.75 m/s for this case of offset.

From Fig. 25b, we can see that the non-oscillatory instability speed does not change with the piezoelectrically induced stresses. On the other hand, the non-oscillatory instability speed is sensitive to the piezoelectric unit position along the span due to the local stiffness and mass change, presenting the lowest value when it is located at the center of the wingspan.

According to Fig. 25c, it can be seen that the higher effectiveness of the piezoelectric unit in improving the structure aeroelastic stability is obtained when an input voltage of 50 V is applied, resulting in an effectiveness parameter of 0.64. The worse case, in turn, is obtained when -50 V is applied, corresponding to an effectiveness of -0.84. In addition, it can be seen that the effectiveness of the piezoelectric unit is not significantly affected by its position along the span.

Changing the ballast offset to -15 mm, we obtain the modal and aeroelastic responses as illustrated in Figs. 26 and 27, respectively.

According to Fig. 26a, the first bending frequency distribution as a function of piezoelectric unit position and prescribed voltage is quite similar to that obtained for the offset case of 0 mm (see Fig. 24a). Moreover, changing the ballast offset to -15 mm, we obtain a range of frequency of 7.31 Hz.

According to Fig. 26b, we can see that the torsion mode can be affected by the piezoelectrically induced stresses. As discussed in the previous case of ballast offset, this occurs due to the ballast contribution to the bending-torsion coupling. In addition, it can be seen that the torsion mode frequency is also affected by the different spanwise positions of the piezoelectric unit due to the local stiffness and mass increasing provided by the piezoelectric material. As can be seen, a range of frequency of 2.81 Hz was obtained prescribing voltages from -200 V to 200 V.

As can be seen in Fig. 27a, a completely different flutter speed distribution as a function of piezoelectrically induced stresses is obtained by allocating the ballast at the leading edge. The highest flutter speeds are obtained by allocating the piezoelectric unit at the center of the wingspan and prescribing negative voltages. Conversely, the lowest flutter speeds are obtained by allocating the piezoelectric unit near the boundaries and prescribing positive voltages. As can be seen, a range of flutter speed of 21.00 m/s was obtained prescribing voltages from -200 V to 200 V.

As illustrated in Fig. 27b, the non-oscillatory instability speed is not affected by the piezoelectric induced stresses. As can be seen, the speed distribution is equal to that observed for the offset case of 0 mm, indicating that the change of mass distribution did not affect this aeroelastic instability. Therefore, taking into account the analysis performed in Section 4.2.1, we can assure that the non-oscillatory instability described in Figs. 25b and 27b is the static divergence of the structure under study.

According to Fig. 27c, it can be seen that the higher effectiveness of the piezoelectric unit in improving the structure aeroelastic stability is obtained when an input voltage of -50 V is applied ($\eta = 0.19$), while the worse case is obtained for an input voltage of 50 V ($\eta = 0.20$). Therefore, it can be seen that the piezoelectric unit effectiveness tendency can practically invert by simply moving the ballast position towards the leading edge. Moreover, its position along the span turns to present more influence on the effectiveness parameter.

Changing the ballast offset to 15 mm, we obtain modal and aeroelastic responses as illustrated in Figs. 28 and 29, respectively.

According to Fig. 28, setting the offset to 15 mm, we obtain the same modal response obtained in the previous case, as can be seen by comparing Figs. 26 and 28. This is already expected since these ballast offsets represent the same case from the

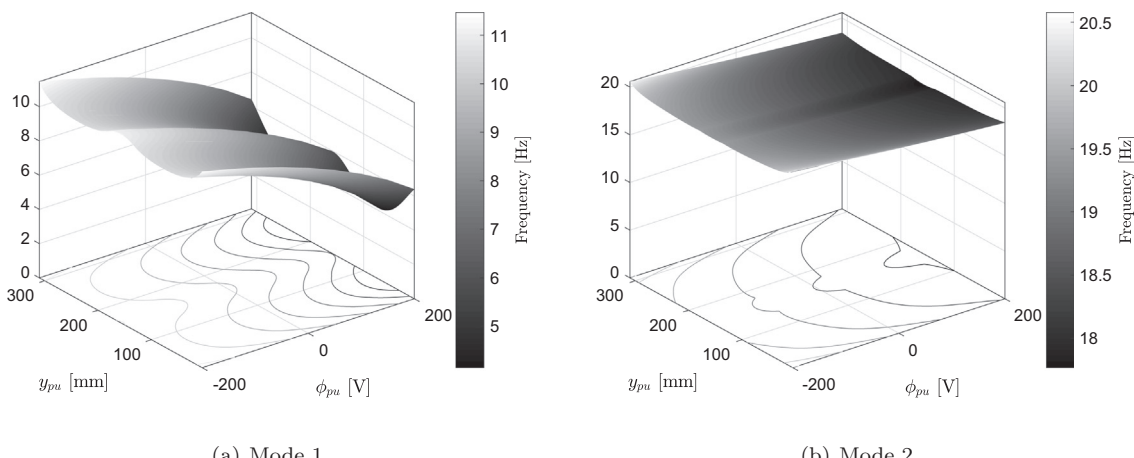


Fig. 26. Modal analysis for different piezoelectric unit spanwise positions y_{pu} and input voltages ϕ_{pu} , considering $L = 35$ cm, layup $[(0, 90)_3]$ and ballast located at the middle of the span with offset equal to -15 mm.

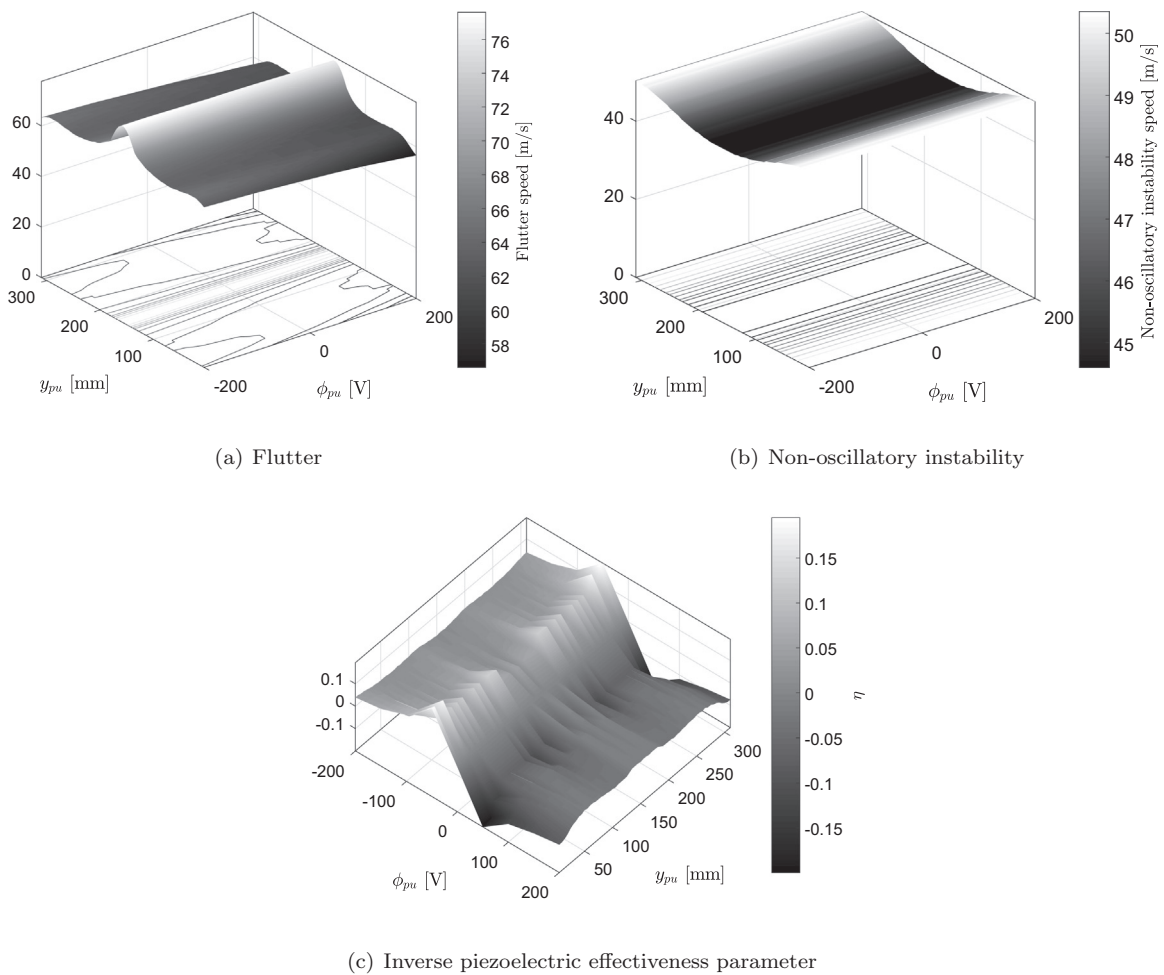


Fig. 27. Aeroelastic analysis for different piezoelectric unit spanwise positions y_{pu} and input voltages ϕ_{pu} , considering $L = 35$ cm, layup $[(0, 90)_3]$ and ballast located at the middle of the span with offset equal to -15 mm.

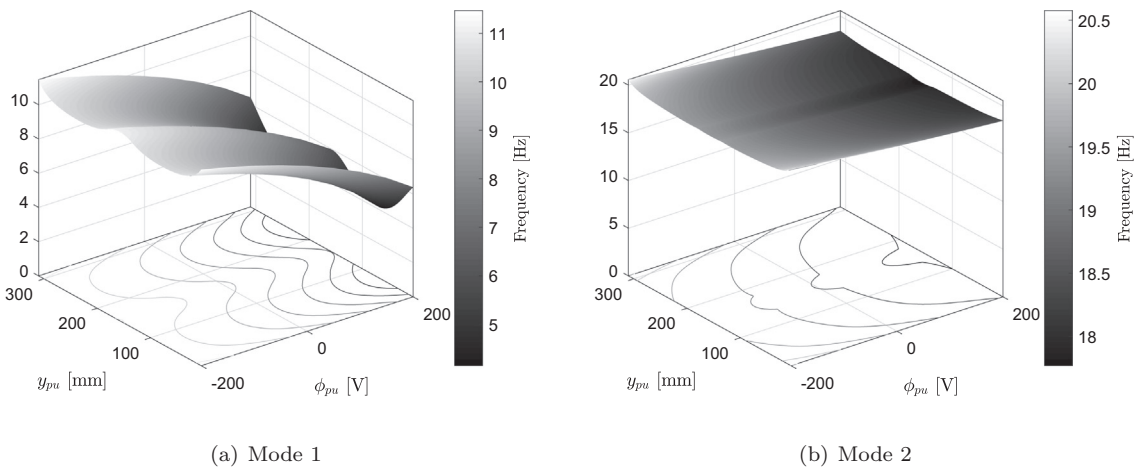


Fig. 28. Modal analysis for different piezoelectric unit spanwise positions y_{pu} and input voltages ϕ_{pu} , considering $L = 35$ cm, layup $[(0, 90)_3]$ and ballast located at the middle of the span with offset equal to 15 mm.

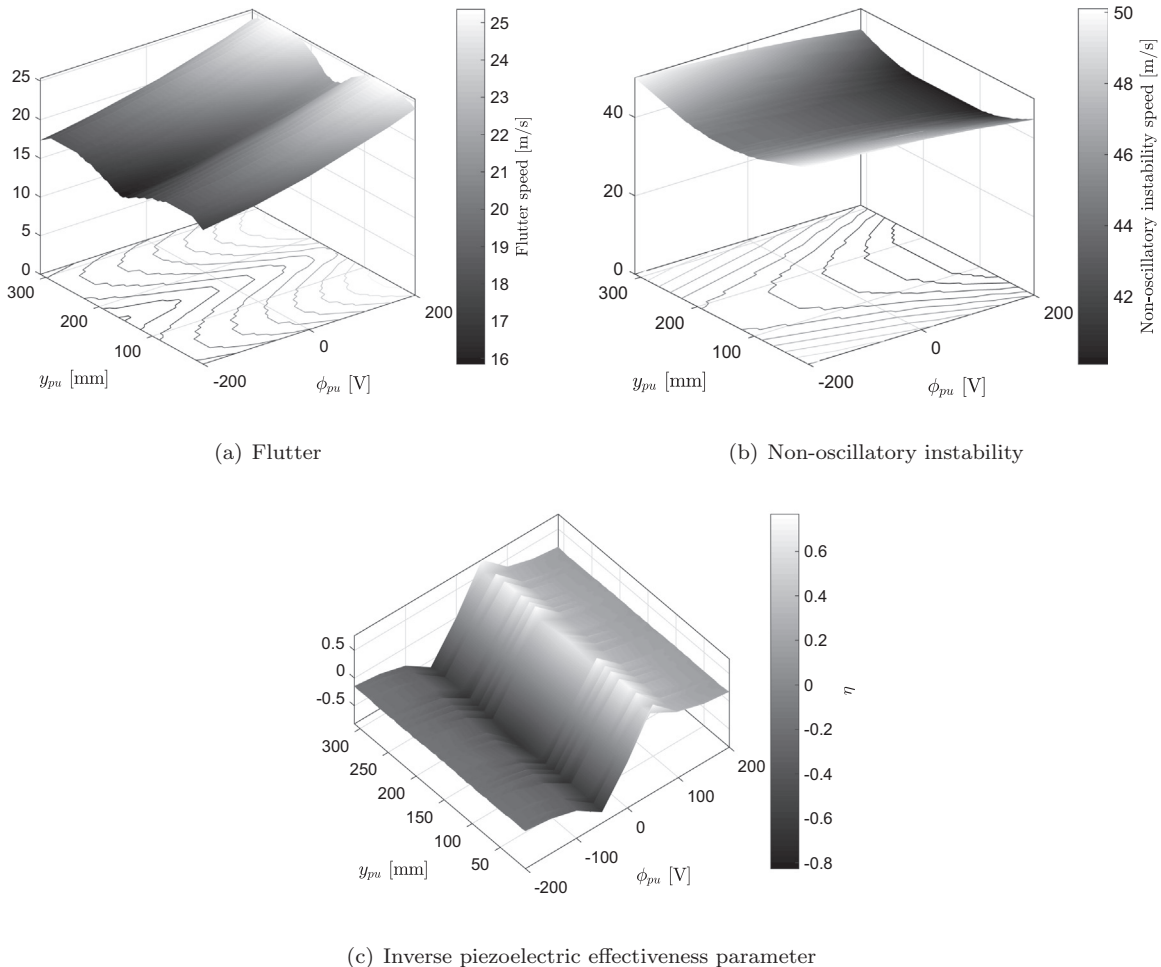


Fig. 29. Aeroelastic analysis for different piezoelectric unit spanwise positions y_{pu} and input voltages ϕ_{pu} , considering $L = 35$ cm, layup $[(0, 90)_3]$ and ballast located at the middle of the span with offset equal to 15 mm.

free vibration point of view. Therefore, piezoelectrically induced stresses will induce the same modal responses in both cases.

From the aeroelastic stability point of view, in turn, these two symmetrical positions of ballast along the chord provide different aeroelastic responses when piezoelectrically induced stresses are present, as can be observed by comparing Figs. 27 and 29.

According to Fig. 29a, the flutter speed distribution as a function of piezoelectrically induced stresses is similar to that obtained for the offset case of 0 mm (see Fig. 25a). In the present case, the highest flutter speeds are also reached when the piezoelectric unit assumes the positions and prescribed voltages which correspond to the lowest first bending frequencies and the lowest flutter speeds are obtained when the piezoelectric unit assumes the positions and prescribed voltages which correspond to the highest first bending frequencies. In the present case, a range of flutter speed of 9.50 m/s was obtained prescribing voltages from -200 V to 200 V.

According to Fig. 29b, it can be seen that the non-oscillatory instability presents a different speed distribution from the two previous offset cases when piezoelectrically induced stresses are acting on the structure. This difference would be expected because, as discussed in Section 4.2.1, the *post-flutter divergence* speed is lower than the static divergence speed when the ballast is positioned at the trailing edge (see Fig. 19). Furthermore, since the *post-flutter divergence* speed depends on the mass distribution, the inertial contribution of the piezoelectric unit would already change the respective aeroelastic response. In addition, since flutter occurs due to first bending and first torsion coupling (see Sections 4.1 and 4.2.1) and the piezoelectrically induced stresses affect both modes for this case of offset (see Figs. 28), the *post-flutter divergence* speed will also be affected by the piezoelectrically induced stresses.

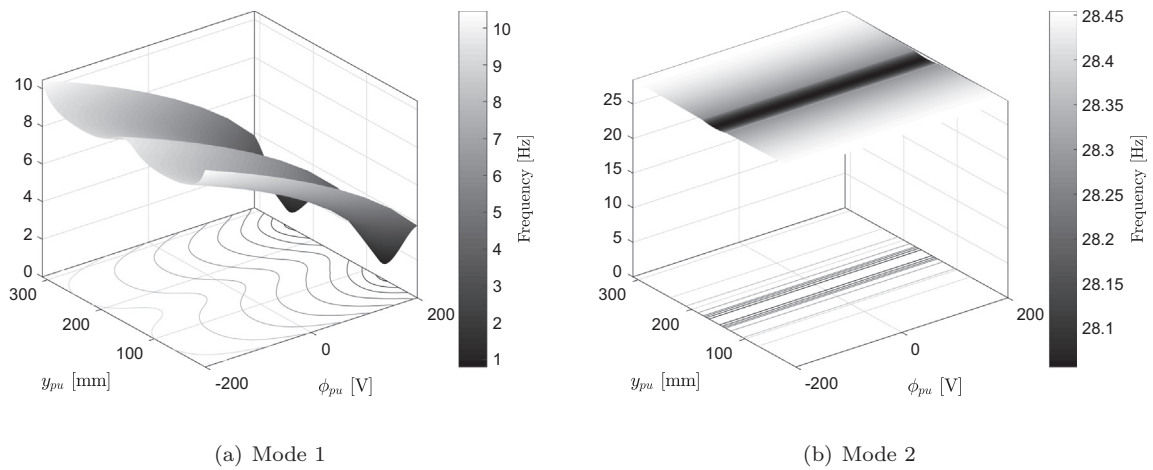


Fig. 30. Modal analysis for different piezoelectric unit spanwise positions y_{pu} and input voltages ϕ_{pu} , considering $L = 35$ cm, layup $[(-45, 45)_3]$ and ballast located at the middle of the span with offset equal to 0 mm.

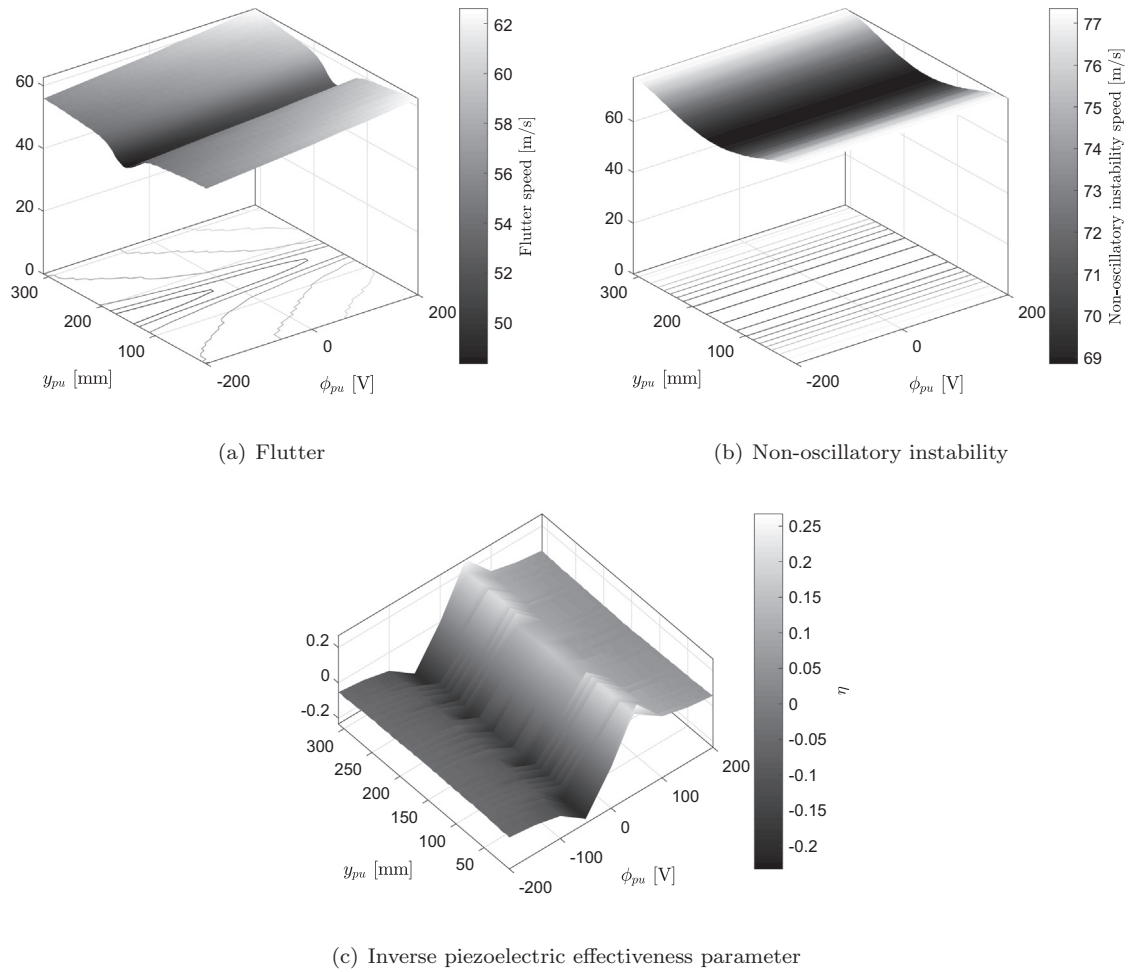


Fig. 31. Aeroelastic analysis for different piezoelectric unit spanwise positions y_{pu} and input voltages ϕ_{pu} , considering $L = 35$ cm, layup $[(-45, 45)_3]$ and ballast located at the middle of the span with offset equal to 0 mm.

According to Fig. 29c, it can be seen an effectiveness parameter tendency similar to the case when the ballast offset is equal to 0 mm, with higher value when $\phi_{pu} = 50$ V ($\eta = 0.77$) and lower value when $\phi_{pu} = -50$ V ($\eta = -0.83$). Moreover, the effectiveness parameter is not significantly affected by the piezoelectric unit position along the span.

4.3.2. Laminate $[(-45, 45)_3]$

As a second case of laminate layup, consider a plate-like wing with stacking sequence $[(-45, 45)_3]$ and ballast offset equal to 0 mm, whose modal and aeroelastic analyses are illustrated in Figs. 30 and 31, respectively.

According to Fig. 30a, the first bending frequency distribution due to the piezoelectrically induced stresses is similar to that obtained for the layup case $[(0, 90)_3]$ (see Fig. 24a). However, observing the frequency distribution for the first bending mode, specially comparing the frequencies obtained for ± 200 V with those obtained for 0 V, it becomes clearer that the piezoelectrically induced stresses due to positive input voltages affect more the higher shear regions, whereas negative input voltages affect more the higher bending regions, as observed by Kuo [7]. As can be seen, a range of frequency of 9.66 Hz was obtained.

According to Fig. 30b, the torsion mode is not affected by piezoelectrically induced stresses. However, the increase of local stiffness and mass due to the presence of the piezoelectric material is able to change the torsion frequency when the piezoelectric unit is allocated along the wing span, where a range of frequency of 0.39 Hz was obtained. Therefore, the frequency distribution is quite similar to that observed in the layup case $[(0, 90)_3]$ (see Fig. 24b).

Observing Fig. 31a, we can see that, despite the fact that the modal responses are similar to those obtained for the layup case $[(0, 90)_3]$ (see Fig. 24), the flutter speed due to the piezoelectrically induced stresses presents a different distribution. The highest flutter speed is reached when the piezoelectric unit is allocated at the boundaries prescribing positive voltages. The lowest flutter speeds, in turn, are obtained when the piezoelectric unit assumes the central spanwise position and negative voltages are prescribed. Since these two cases differ only in the fibers orientation angle, the difference between the flutter speed distributions depicted in Figs. 25a and 31a is due to the stacking sequence of the plate-like wing. Moreover, the change of the laminate layup provided a range of flutter speed of 14.25 m/s when piezoelectrically induced stresses are applied.

According to Fig. 31b, the non-oscillatory instability speed distribution does not change with the piezoelectrically induced stresses and is sensitive to the piezoelectric unit position along the span due to the local change of stiffness and mass provided by the piezoelectric material. Moreover, it can be seen that the lowest value is reached when the piezoelectric unit is located at the center of the wingspan. Comparing Figs. 25b and 31b, we can see that the two non-oscillatory instability speed distributions are quite similar. However, in the present case, a range of speeds of 8.50 m/s was obtained.

According to Fig. 31c, it can be seen an effectiveness tendency similar to that present in the case of layup $[(0, 90)_3]$. However, the effectiveness parameter values become quite low, with $\eta = 0.27$ when $\phi_{pu} = 50$ V and $\eta = -0.23$ when $\phi_{pu} = -50$ V.

Changing the ballast offset to -15 mm, we obtain modal and aeroelastic responses as illustrated in Figs. 32 and 33, respectively.

As can be seen in Fig. 32a, the modal response of the first bending mode due to the piezoelectrically induced stresses is quite similar to that observed for the offset case of 0 mm (see Fig. 30a), however it is considerably different from the case of laminate layup $[(0, 90)_3]$ (see Fig. 26a). In the present case, a range of frequency of 9.38 Hz was obtained.

According to Fig. 32b, we can see that the torsion mode can be affected by the piezoelectrically induced stresses due to the ballast contribution to the bending-torsion coupling. Due to the local stiffness and mass increase caused by the presence

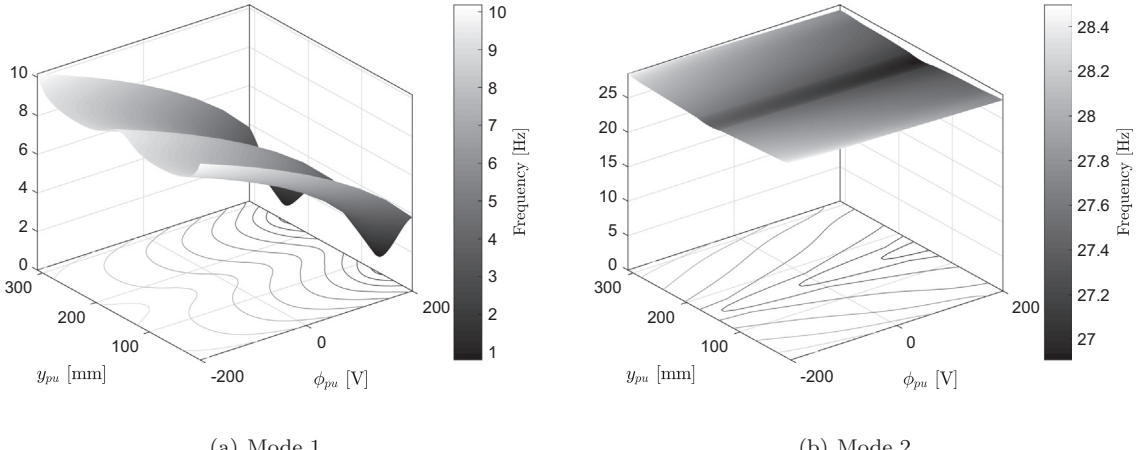


Fig. 32. Modal analysis for different piezoelectric unit spanwise positions y_{pu} and input voltages ϕ_{pu} , considering $L = 35$ cm, layup $[(-45, 45)_3]$ and ballast located at the middle of the span with offset equal to -15 mm.

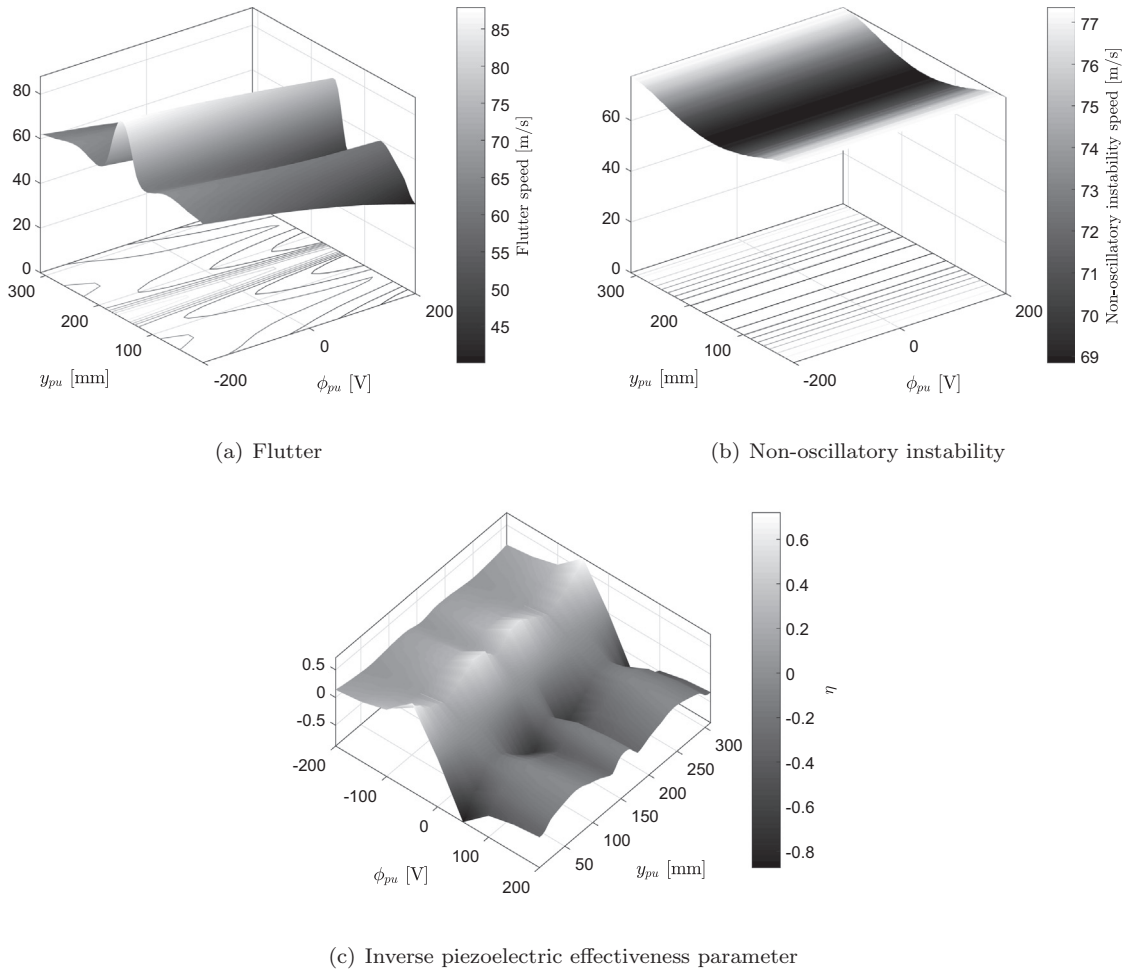


Fig. 33. Aeroelastic analysis for different piezoelectric unit spanwise positions y_{pu} and input voltages ϕ_{pu} , considering $L = 35$ cm, layup $[(−45, 45)_3]$ and ballast located at the middle of the span with offset equal to -15 mm.

of the piezoelectric material, the torsion mode frequency is also affected by the different spanwise positions of the piezoelectric unit. As can be seen, a range of frequency of 1.59 Hz was obtained prescribing voltages from -200 V to 200 V.

As can be seen in Fig. 33a, the highest flutter speeds are obtained by allocating the piezoelectric unit at the center of the wingspan and prescribing negative voltages while the lowest flutter speeds are obtained by allocating the piezoelectric unit at the boundaries and prescribing positive voltages. In this case, a range of flutter speed around 47.75 m/s was obtained prescribing voltages from -200 V to 200 V.

According to Fig. 33b, the speed distribution is equal to that observed for the offset case of 0 mm, indicating that the change of mass distribution did not affect this aeroelastic instability. Similar to that observed for the layup case $[(0, 90)_3]$, we can take into account the analysis performed in Section 4.2.2 to assure that the non-oscillatory instability described in Figs. 31b and 33b is the static divergence of the structure under study.

According to Fig. 33c, it can be seen that, as observed for the layup case of $[(0, 90)_3]$, the effectiveness parameter tendency becomes quite different when the ballast center of mass is located towards the leading edge. Here, the highest effectiveness parameter obtained is $\eta = 0.72$ ($\phi_{pu} = -50$ V), while the lowest value is $\eta = -0.87$ ($\phi_{pu} = 50$ V). In addition, it can be seen that the piezoelectric unit position along the span can significantly affect the parameter η .

Changing the ballast offset to 15 mm, we obtain modal and aeroelastic responses as illustrated in Figs. 34 and 35, respectively.

As discussed for the previous laminate layup case, by setting the offset to 15 mm or -15 mm, we obtain the same modal response because these ballast offsets represent the same case from the free vibration point of view. Therefore, piezoelectrically induced stresses will induce the same modal responses in both cases, as can be observed comparing Figs. 32 and 34. However, as already discussed, these two symmetrical positions of ballast along the chord provide different aeroelastic responses when piezoelectrically induced stresses are prescribed, as can be observed by comparing Figs. 33 and 35.

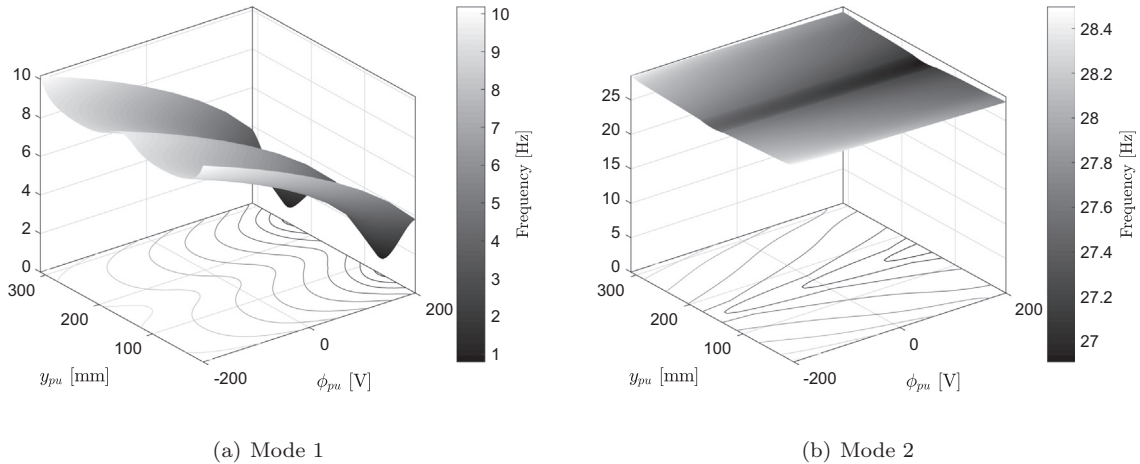


Fig. 34. Modal analysis for different piezoelectric unit spanwise positions y_{pu} and input voltages ϕ_{pu} , considering $L = 35$ cm, layup $[(-45, 45)_3]$ and ballast located at the middle of the span with offset equal to 15 mm.

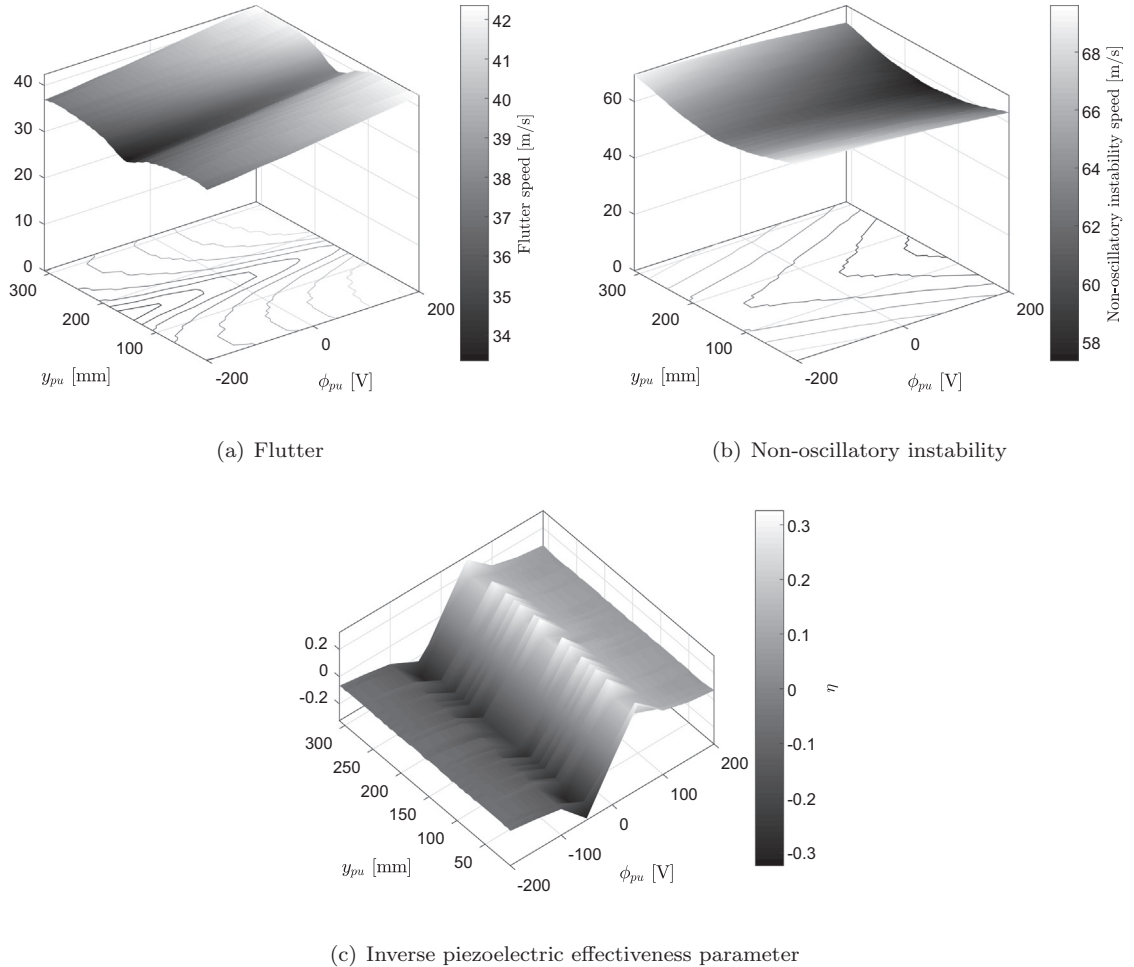


Fig. 35. Aeroelastic analysis for different piezoelectric unit spanwise positions y_{pu} and input voltages ϕ_{pu} , considering $L = 35$ cm, layup $[(-45, 45)_3]$ and ballast located at the middle of the span with offset equal to 15 mm.

Table 9Frequency and speed ranges for the layup case $[(0, 90)_3]$.

		Modal analyses [Hz]			Aeroelastic analyses [m/s]							
Ballast offset		-15	0	15		-15	0	15		-15	0	15
max	Mode 1	11.46	13.09	11.46	Flutter	77.60	35.60	25.35	η	0.19	0.64	0.77
		4.15	4.19	4.15		56.60	22.85	15.85		-0.20	-0.84	-0.83
		7.31	8.90	7.31		21.00	12.75	9.50		0.39	1.48	1.60
min	Mode 2	20.58	18.48	20.58	Non-osc. inst.	50.35	50.35	50.10				
		17.77	18.19	17.77		44.60	44.60	40.10				
		2.81	0.29	2.81		5.75	5.75	10.00				

Table 10Frequency and speed ranges for the layup case $[(-45, 45)_3]$.

		Modal analyses [Hz]			Aeroelastic analyses [m/s]							
Ballast offset		-15	0	15		-15	0	15		-15	0	15
max	Mode 1	10.18	10.46	10.18	Flutter	87.85	62.60	42.35	η	0.72	0.27	0.33
		0.80	0.80	0.80		40.10	48.35	33.35		-0.87	-0.23	-0.32
		9.38	9.66	9.38		47.75	14.25	9.00		1.59	0.50	0.65
min	Mode 2	28.50	28.45	28.50	Non-osc. inst.	77.35	77.35	69.60				
		26.91	28.06	26.91		68.85	68.85	57.35				
		1.59	0.39	1.59		8.50	8.50	12.25				

According to Fig. 35a, we can see that higher flutter speeds are obtained when the piezoelectric unit is allocated near the boundaries prescribing positive voltages. On the other hand, the lowest flutter speeds are reached when the piezoelectric unit is allocated at the center of the wingspan and a negative voltage is prescribed. In this case, a range of speed of 9.00 m/s was obtained.

According to Fig. 35b, it can be seen that the non-oscillatory instability presents a different speed distribution from the two previous offset cases when piezoelectrically induced stresses are prescribed. Since in the present case the *post-flutter divergence* speed is lower than the static divergence speed (see Section 4.2.2), it would be expected that the piezoelectric induced stresses and piezoelectric unit spanwise position would affect the non-oscillatory instability speed, as discussed for the previous case of laminate layup. In the present case, the highest values of *post-flutter divergence* speeds are obtained when the piezoelectric unit is allocated at the boundaries prescribing negative voltages, while the lowest speeds are reached when it is positioned at the center of the wingspan prescribing positive voltages. As can be seen, a range of speed of 12.25 m/s was obtained.

According to Fig. 35c, it can be seen an effectiveness parameter tendency similar to the case when the ballast offset is equal to 0 mm, with highest value when $\phi_{pu} = 50$ V ($\eta = 0.33$) and lowest value when $\phi_{pu} = -50$ V ($\eta = -0.32$). In this case, the effectiveness parameter is not significantly affected by the piezoelectric unit position along the span.

Gathering all the results obtained in this section, the maximum and minimum values of frequency and speed, as well as the respective ranges and inverse piezoelectric effectiveness parameter, can be listed as described in Tables 9 and 10.

In terms of modal response, the first mode of the layup case $[(-45, 45)_3]$ showed to be more sensitive to piezoelectrically induced stresses than the case $[(0, 90)_3]$, specially when the ballast presents an offset equal to 0 mm. However, the second mode becomes more sensitive when the structure assumes the layup $[(0, 90)_3]$, specially when the ballast offset is equal to ± 15 mm.

In terms of aeroelastic response, it can be seen that the highest flutter speed is obtained when the layup is $[(-45, 45)_3]$ and the ballast is positioned with offset equal to -15 mm, i.e., towards the leading edge. Moreover, this configuration also presented the highest flutter speed range, showing to be the most sensitive to piezoelectrically induced stresses.

In terms of inverse piezoelectric effectiveness parameter, the highest value is obtained when the layup is $[(0, 90)_3]$ and the ballast is positioned with offset equal to 15 mm, i.e., towards the trailing edge. However, the second highest value is obtained when the layup is $[(-45, 45)_3]$ and the ballast is positioned with offset equal to -15 mm, i.e., towards the leading edge.

5. Conclusions

The aeroelastic behavior of a composite plate-like wing under piezoelectrically induced stresses has been addressed in this paper. In addition, parametric studies were also performed investigating the influence of aspect ratio, fibers orientation angle, ballast spanwise position and its offset along the chord, as well as piezoelectric unit position along the span and its input voltage.

A model employing smart beam elements and time domain aerodynamic loads with strip theory for stress stiffening aeroelastic problems was developed and carefully validated. The model takes into account the stiffness and inertial contri-

butions provided by the piezoelectric transducers attached to the host structure and the bending-torsion coupling provided by the ballast located at different positions along the span and chord, in order to simulate the inertial contribution of additional devices usually attached to wings, as missiles and engines.

Results show that the electromechanical structure can present quite different aeroelastic responses depending on the configuration of the investigated parameters. Therefore, a structure can have its aeroelastic stability improved simply by tuning its mechanical properties appropriately. The aeroelastic stability is significantly improved when the layup is $[(-45, 45)_3]$, due to the higher bandwidth obtained between the two modes involved in the flutter mechanism. Even though this improvement was observed on all cases of aspect ratio considered, the flutter and divergence speeds are less affected by the fiber orientation angle as the aspect ratio increases. In addition, it was seen that when attaching a device to the structure, its center of mass is desired to be located around the center of the span or near the clamped extremities, and towards the leading edge.

Post-flutter divergence speeds lower than the static divergence speeds were detected for some special cases of structural mass distribution. Therefore, in order to correctly evaluate the aeroelastic response of structures similar to those studied in this work, the non-oscillatory instabilities have to be carefully analyzed.

In addition, a technological solution through piezoelectrically induced stresses was proposed in order to improve the aeroelastic stability of high aspect ratio bi-clamped wings. Results showed a promising performance of such technique, since it could increase the bandwidth of two flexible modes associated with the flutter mechanism. Therefore, the piezoelectric unit position and the magnitude of the prescribed voltage can be conveniently modified in order to reach higher flutter and divergence speeds. The magnitude of piezoelectrically induced stresses influence on modal response is quite similar for both layups considered, which can be seen by comparing the obtained frequency ranges. However, the stacking sequence containing fiber angles equal to 45° provided the highest flutter and divergence speeds as well as the highest range of such speeds, showing to be a potential configuration of structure to be used for piezoelectrically induced stresses application.

Since the results provide an indication of which configuration of mass distribution, level of flexibility, fiber direction and piezoelectric unit position could produce the better performance, it is important to mention that the effectiveness of this technique on a different structure will need to be evaluated case by case, because it will certainly depend on many factors, e.g., the transducers power, covered area, amount of energy available, level of forces involved and specially the electronics required to activate the actuators, due to its relative high voltage of operation.

Funding

This work received financial support from the Comissão de Aperfeiçoamento de Pessoal de Nível Superior (CAPES-PROEX/ITA: process No. 88887.313354/2019-00), Conselho Nacional de Desenvolvimento Científico e Tecnológico (CNPq: process No. 301053/2016-2) and Financiadora de Estudos e Projetos (FINEP: process No. 0114 018300), and technical support from the Instituto de Pesquisas Tecnológicas do Estado de São Paulo (IPT) and Fundação de Apoio ao Instituto de Pesquisas Tecnológicas (FIPT).

Declaration of Competing Interest

The authors declare that they have no known competing financial interests or personal relationships that could have appeared to influence the work reported in this paper.

References

- [1] A.R. Faria, On buckling enhancement of laminated beams with piezoelectric actuators via stress stiffening, *Compos. Struct.* 65 (2) (2004) 187–192.
- [2] Y. Fridman, H. Abramovich, Enhanced structural behavior of flexible laminated composite beams, *Compos. Struct.* 82 (1) (2008) 140–154.
- [3] K. Kulínski, J. Przybylski, Stability and vibrations control of a stepped beam using piezoelectric actuation, in: MATEC Web of Conferences, EDP Sciences, vol. 157, 2018.
- [4] M.V. Donadon, S.F.M. Almeida, A.R. Faria, Stiffening effects on the natural frequencies of laminated plates with piezoelectric actuators, *Compos. Part B: Eng.* 33 (5) (2002) 335–342.
- [5] H. Waisman, H. Abramovich, Active stiffening of laminated composite beams using piezoelectric actuators, *Compos. Struct.* 58 (1) (2002) 109–120.
- [6] H. Waisman, H. Abramovich, Variation of natural frequencies of beams using the active stiffening effect, *Compos. Part B: Eng.* 33 (6) (2002) 415–424.
- [7] S.Y. Kuo, Stiffening effects on the natural frequencies of laminated beams with piezoelectric actuators, *J. Aeronaut. Astronaut. Aviation* 42 (2010) 67–72.
- [8] M.M. Kaseem, E.H. Dowell, A study of the natural modes of vibration and aeroelastic stability of a plate with a piezoelectric material, *Smart Mater. Struct.* 27 (7) (2018).
- [9] M.M. Kaseem, H. Negm, A. Elsabbagh, Aeroelastic modeling of smart composite wings using geometric stiffness, *J. Aerospace Eng.* 32 (2) (2018).
- [10] M.K. Bradley, C.K. Dorney, Subsonic ultra green aircraft research, 2011.
- [11] NASA, Lockheed Martin.https://www.nasa.gov/sites/default/files/composite_1a_original_full_0.jpg, 2019. [Online; accessed 21-July-2019].
- [12] J.N. Reddy, Mechanics of Laminated Composite Plates and Shells: Theory and Analysis, CRC Press, 2003.
- [13] R.C. Hibbeler, Mechanics of Materials, eighth ed., Pearson Prentice Hall, 2011.
- [14] T.S.S. Versiani, F.J. Silvestre, A.B. Guimarães Neto, D.A. Rade, R.G.A. Silva, M.V. Donadon, R.M. Bertolin, G.C. Silva, Gust load alleviation in a flexible smart idealized wing, *Aerospace Sci. Technol.* 86 (2019) 762–774.
- [15] B.G. Sinir, B.B. Özhan, J.N. Reddy, Buckling configurations and dynamic response of buckled Euler-Bernoulli beams with non-classical supports, *Latin Am. J. Solids Struct.* 11 (14) (2014) 2516–2536.
- [16] Y.G. Wang, H.F. Song, W.H. Lin, J.K. Wang, Large amplitude free vibration of micro/nano beams based on nonlocal thermal elasticity theory, *Latin Am. J. Solids Struct.* 12 (10) (2015) 1918–1933.

- [17] D.J. Leo, Engineering Analysis of Smart Material Systems, John Wiley & Sons, 2007.
- [18] J.A. Hernandes, S.F.M. Almeida, A. Nabarrete, Stiffening effects on the free vibration behavior of composite plates with pzt actuators, *Compos. Struct.* 49 (1) (2000) 55–63.
- [19] Y.C. Fung, An Introduction to the Theory of Aeroelasticity, Courier Dover Publications, 2008.
- [20] F.J. Silvestre, R. Luckner, Experimental validation of a flight simulation model for slightly flexible aircraft, *AIAA J.* 53 (12) (2015) 3620–3636.
- [21] M.N. Bismarck-Nasr, Structural Dynamics in Aeronautical Engineering, American Institute of Aeronautics and Astronautics, 1999.
- [22] J.R. Wright, J.E. Cooper, Introduction to Aircraft Aeroelasticity and Loads, vol. 20, John Wiley & Sons, 2008.
- [23] R.L. Bisplinghoff, H. Ashley, R.L. Halfman, Aeroelasticity, Dover Publications, 1996.
- [24] J.R. Ray, Modified Hamilton's principle, *Am. J. Phys.* 41 (10) (1973) 1188–1190.
- [25] A. Alves Filho, Elementos Finitos—A base da tecnologia CAE, Editora Saraiva, 2018.
- [26] A. Suleman, V.B. Venkayya, A simple finite element formulation for a laminated composite plate with piezoelectric layers, *J. Intell. Mater. Syst. Struct.* 6 (6) (1995) 776–782.
- [27] W.S. Hwang, H.C. Park, Finite element modeling of piezoelectric sensors and actuators, *AIAA J.* 31 (5) (1993) 930–937.
- [28] C.M. Wang, C.Y. Wang, Exact Solutions for Buckling of Structural Members, CRC Press, 2004.
- [29] W.P. Rodden, E.D. Bellinger, Aerodynamic lag functions, divergence, and the british flutter method, *J. Aircraft* 19 (7) (1982) 596–598.
- [30] A. Almeida, M.V. Donadon, A.R. de Faria, S.F.M. de Almeida, The effect of piezoelectrically induced stress stiffening on the aeroelastic stability of curved composite panels, *Compos. Struct.* 94 (12) (2012) 3601–3611.